Design of sand-based, 3D-printed analogue faults with controlled frictional properties

Philipp Braun[1], Georgios Tzortzopoulos[1], and Ioannis Stefanou[1]

[1]Ecole Centrale de Nantes

November 26, 2022

Abstract

Laboratory experiments with surrogate materials play an important role in fault mechanics. They allow improving the current state of knowledge by testing various scientific hypotheses in a repeatable and controlled way. Central in these experiments is the selection of appropriate analogue, rock-like materials. Here we investigated the frictional properties of sand-based, 3D-printed materials. Pursuing further recent experimental works, we performed detailed uniaxial compression tests, direct shear and inclined plane tests in order to determine a) the main bulk mechanical parameters of this new analogue material, b) its viscous behavior, c) its frictional properties and d) the influence of some printing parameters. Complete stress-strain / apparent friction-displacement curves were presented including the post-peak, softening behavior, which is a key factor in earthquake instability. Going a step further, we printed rock-like interfaces of custom frictional properties. Based on a simple analytical model, we designed the a) maximum, minimum and residual apparent frictional properties, b) characteristic slip distance (d_c), c) evolution of the friction coefficient with slip and d) dilatancy of the printed interfaces. This model was experimentally validated using interfaces following a sinusoidal pattern, which led to an oscillating evolution of the apparent friction coefficient with slip. This could be used for simulating the periodical rupture and healing of fault sections. Additionally, our tests showed the creation of a gouge-like layer due to granular debonding during sliding, whose properties were quantified. The experimental results and the methodology presented make it possible to design new surrogate laboratory experiments for fault mechanics and geomechanics.

Design of sand-based, 3D-printed analogue faults with controlled frictional properties

P. Braun[1], G. Tzortzopoulos[1], I. Stefanou[1]

[1]Institut de Recherche en Génie Civil et Mécanique, Ecole Centrale de Nantes
1 Rue de la Noë, Nantes 44321, France

Key Points:

- We design and test analogue fault interfaces using 3D-printing with sand particles
- We control the evolution of the friction coefficient with slip, by adequately designing the printed interface geometry
- Wear and gouge production is enhanced by adjusting the 3D-printing settings

Corresponding author: Philipp Braun, `philipp.braun@enpc.fr`

Abstract

Laboratory experiments with surrogate materials play an important role in fault mechanics. They allow improving the current state of knowledge by testing various scientific hypotheses in a repeatable and controlled way. Central in these experiments is the selection of appropriate analogue, rock-like materials. Here we investigated the frictional properties of sand-based, 3D-printed materials. Pursuing further recent experimental works, we performed detailed uniaxial compression tests, direct shear and inclined plane tests in order to determine a) the main bulk mechanical parameters of this new analogue material, b) its viscous behavior, c) its frictional properties and d) the influence of some printing parameters. Complete stress-strain / apparent friction-displacement curves were presented including the post-peak, softening behavior, which is a key factor in earthquake instability.

Going a step further, we printed rock-like interfaces of custom frictional properties. Based on a simple analytical model, we designed the a) maximum, minimum and residual apparent frictional properties, b) characteristic slip distance (d_c), c) evolution of the friction coefficient with slip and d) dilatancy of the printed interfaces. This model was experimentally validated using interfaces following a sinusoidal pattern, which led to an oscillating evolution of the apparent friction coefficient with slip. This could be used for simulating the periodical rupture and healing of fault sections. Additionally, our tests showed the creation of a gouge-like layer due to granular debonding during sliding, whose properties were quantified. The experimental results and the methodology presented make it possible to design new surrogate laboratory experiments for fault mechanics and geomechanics.

1 Introduction

The slow movement of tectonic plates continuously accumulates elastic energy in the earth's crust, which is suddenly released during earthquakes. A small part of this energy travels up to the surface in the form of seismic waves, which have catastrophic results for our built and shaped environment (Jones, 2018). Nevertheless, most of the energy is dissipated in the fault zone due to friction. Friction determines the nucleation of an earthquake, the evolution of seismic slip and the magnitude of seismic events (Scholz, 2002). Understanding friction is therefore a key element for studying earthquake nucleation, its possible mitigation and control (e.g. Raleigh et al., 1976; Barbot et al., 2012; Popov et al., 2012; Edwards et al., 2015; Bommer et al., 2006; Stefanou, 2019). Central in building understanding of induced/triggered earthquakes and their potential mitigation are in-situ measurements and laboratory testing.

Several experimental approaches have been developed for reproducing earthquakes in the laboratory. Laboratory experiments involve testing of natural rocks or rock-like, surrogate materials (e.g. Brace & Byerlee, 1966; Dieterich, 1979, 1981; Power et al., 1988). A large variety of analogue materials has been employed in the literature. For instance, we refer to experiments with glass beads (Anthony & Marone, 2005), rubber (Schallamach, 1971), foam rubber (Brune, 1973), sandpaper (King, 1975), cardboard (Heslot et al., 1994), and pasta (Knuth & Marone, 2007), among others (see Rosenau et al., 2017, for a comprehensive overview). Analogue materials permit not only to have better control over different parameters, but also to produce numerous specimens for repeatable experiments. *Repeatability* and *falsifiability* are of paramount importance for testing any theory or conjecture. This is especially important for systems where direct measurements are difficult to obtain or contain multiple sources of error. In this work, we propose a new analogue material for fault experiments, which enables the design of the apparent frictional parameters of rock-like frictional interfaces. This is achieved using 3D-printing with sand particles. This novel approach gives the advantage of controlling several properties such as the roughness, the exact geometry of the asperities, the maximum and minimum apparent friction coefficient, the exact evolution of friction with slip and the characteristic slip distance, d_c of the frictional interfaces.

In the literature, experiments on rock friction have not only been of interest in fault mechanics, but also in wider geo-engineering applications such as the stability in tunnelling and slopes. One can find a large number of studies discussing the contribution of joint roughness and asperities to the shear resistance of rocks, following the pioneering works of Newland and Allely (1957); Patton (1966). Analogue specimens have been created in this regard, as for instance for investigating the effects of triangle-shaped asperities on the shear resistance (Huang et al., 2002). These authors tested specimens made of a mix of chalk, sand and water, and analysed the observed asperity friction and asperity cut-off in a theoretical model. Moreover, Asadi et al. (2013); Indraratna et al. (2015) showed experimentally on synthetic rocks, that the joint friction can be significantly reduced by asperity damage.

Analogue interfaces, resembling more closely the geometry of natural rocks, have been replicated by 3D-printed molds (e.g. Fang et al., 2018) or 3D-printed acrylic resin specimens (Ishibashi et al., 2020). The aforementioned analogue materials permitted to carry out laboratory experiments and to infer properties that occur in real faults. Moreover, they allowed one to explore the mechanisms behind various phenomena, such as asperity damage and gouge material creation, and their effect on apparent friction.

Here we go beyond that approach by taking key fault characteristics and scale them down to the lab scale. These key properties can be local parameters, or average properties of an entire fault area, obtained through geodetic and seismological measurements. We use a recently developed, analogue, composite material, which gives a large scope for adjusting composition and micro-structural behavior of analogue rock-like frictional interfaces. More specifically, we employ sand-based 3D-printing, which enables us to adjust the geometry and roughness of analogue fault interfaces. Using Patton's considerations on roughness (Patton, 1966), we succeed in generating desired frictional properties and reproduce the effects of asperity breakage and fault gouge creation. The latter is possible thanks to the applied 3D-printing technology, which uses sand particles of controlled size connected through resin bonds, that can break during shearing. Moreover, sand-based 3D-printing allows us to control the post-peak characteristic slip distance d_c, which, together with the adjustable maximum and residual friction coefficient, enable us to control the frictional dissipation during slip. Note that this is central in the study of the earthquake phenomenon and its triggering (Scholz, 2002; Rattez et al., 2018a, 2018b; Stefanou, 2019).

The paper is organized as follows. In Section 2, we present the employed sand-based 3D-printing technology (S3DP). We characterize the basic mechanical properties of the S3DP material through element tests and investigate how the material composition and printing settings can influence its mechanical behavior. Then, in Section 4, we show how the frictional behavior is directly related to the geometry of the analogue fault asperities and we validate the predicted frictional behavior through experiments. Finally, we discuss advantages, shortcomings, and perspectives of analogue S3DP faults in Section 5.

2 3D-printed analogue rock

2.1 3D-printing technology

We use binder-jetting, a sub-category of 3D-printing technologies, for printing desired geometries of rock-like materials. Binder-jetting allows one to create composite materials by controlled mixing of two components: powder and binder. Among the various potential granular materials, we use here silica sand as the powder component. Before the printing process, silica sand is mixed with an acidic activator. This activator serves

Table 1. Printer settings applied for specimen fabrication.

Silica sand mean grain diameter	140 μm
Binder type	Furfurylic alcohol
Binder content	3.8 or 7.2 wt% of sand
Recoating speed	0.13 or 0.26 m/s
x resolution	20 μm$^{(1)}$ or 40 μm$^{(2)}$
y resolution	101.6 μm
z resolution (layer thickness)	280 μm
Activator content (sulfonic acid)	0.2 wt% of sand
Infra-red curing lamp temperature	32 °C

$^{(1)}$ for high and $^{(2)}$ for low binder content

later as a catalyst for the polymerization reaction of the binder. As shown in Figure 1, a recoater and an inkjet head run over the build platform in alternating sequence. First, the recoater deposits a layer of the sand-activator mixture with a thickness of two times the mean grain diameter D_{50} of silica sand (here D_{50} = 180 μm). At the same time, it applies a small vertical pressure, in order to compact the new layer. Then, the inkjet head drops the binder (Furfurylic alcohol), which reacts with the activator and solidifies. Due to capillary forces, the binder is concentrated at the grain contacts and forms solid bridges, resulting in a rigid sand-binder matrix as depicted in Figures 2a,b. Gravitational forces distribute the binder throughout the new sand layer and ensure binding to the previously deposited layer. Controlled amounts of binder are then deposited on each layer, under a given binder-to-sand ratio. Finally, the building platform moves downwards and a new layer is printed, until the desired geometry is completed (for more details on the printing procedure we refer to Primkulov et al., 2017; Gomez et al., 2019; Mitra, Rodríguez de Castro, & El Mansori, 2019). The shape of the final object, which can be of arbitrary geometry (Figure 2c), is defined through an input CAD model. All principal printer settings for creating the specimens tested in this work are presented in Table 1.

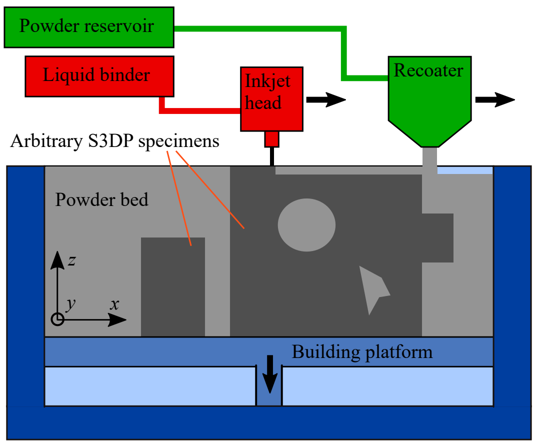

Figure 1. Schematic elements of a 3D printer for powder-binder composites, adapted from Upadhyay et al. (2017).

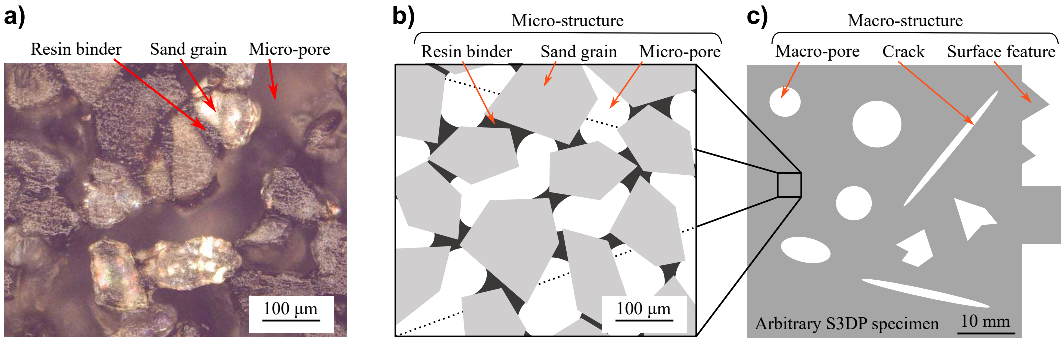

Figure 2. a) Cross section of the S3DP material. b) Schematic representation of the micro-structure and c) of the macro-structure of the S3DP material.

2.2 Micro-mechanical properties and analogies with natural rocks

Specimens created by powder-based 3D-printing are characterized by their micro- and macro-structure (Figure 2). The micro-structure describes the composition of the powder, binder and pore phases, and can be adjusted to a large extent to achieve desired macroscopic mechanical properties. More specifically, the macroscopic mechanical properties of 3D printed analogues based on powder minerals (such as the S3DP material used herein) can be controlled by different process variables. For instance, phase composition, macroporosity and pore geometry have high impact on the compressive strength of 3D-printed specimens (Schumacher et al., 2010). Vaezi and Chua (2011) found that increasing the binder saturation of plaster-powder-based printed materials can improve mechanical resistance. They also observed that an increase of the printing layer thickness reduces the tensile resistance, but increases flexural strength. Moreover, the printing layer orientation induces anisotropy in the microstructure (Vlasea et al., 2015), which can affect the apparent mechanical and hydraulic properties at the macro-scale. While having a minor effect on dimensional accuracy and pore structures, the printing speed can have a significant influence on the strength and structural accuracy of 3D-printed specimens. Farzadi et al. (2015) showed, that very fast printing prevents the binder from spreading and penetrating uniformly, resulting in lower mechanical resistance. Conversely, if printing is carried out too slow, the binder hardens before the subsequent layer is completed, resulting in reduced adhesion between layers, leading to lower resistance. While the binder cures, the application of heat until a certain degree can improve the mechanical properties (Primkulov et al., 2017). Very high temperatures, however, can reduce the mechanical resistance. In addition, ageing, curing time and curing temperature can influence S3DP materials (Mitra et al., 2018).

Mechanical properties of S3DP analogues can be adjusted through the most important printing parameters: a) the printing layer thickness, b) the layer orientation and c) the binder saturation (Gomez et al., 2019). According to Gomez et al. (2019), the printing layer thickness defines the thickness of new material added parallel to the building plane in each printing step. The layer orientation describes the angle between printing layers and loading direction, while the binder saturation denotes the percentage of sand pore volume filled by binder. Moreover, Gomez et al. (2019) have found an increase of uniaxial compressive strength when increasing the binder saturation. On the contrary, when they increased the layer thickness from 220 to 400 μm, they measured a significant decrease of uniaxial compressive strength. Finally, Mitra, Rodríguez de Castro, and El Mansori (2019) noted that a higher recoating speed leads to a lower grain packing density and therefore higher porosity. Furthermore, heterogeneities in density might increase due to the faster distribution of sand.

Even though literature examples of the use of sand-based 3D-printed materials in geomechanics applications are limited, Gomez (2017); Gomez et al. (2019) state that for given sand and binder properties, S3DP materials show similar behavior and mechanical characteristics with natural rocks. For instance, they measured an unconfined compressive strength between approximately 15 and 20 GPa, a Young modulus between 1.6 and 1.9 GPa and a Poisson ratio between 0.19 and 0.25 on S3DP specimens with a porosity between 36 and 47%. These mechanical properties are close to the ones found on weak sandstones, such as the Wildmoor or Waterstone sandstones (compressive strength of approximately 10 and 20 GPa, Young's modulus of around 2 and 7 GPa, porosity of 25%, respectively, according to Dobereiner & Freitas, 1986; Papamichos et al., 2000).

2.3 Printing material composition used in this study

Given the important effects of various printing parameters discussed in the previous section, we chose here to vary only two printing parameters, the recoating speed and the binder saturation. The layer orientation and layer thickness remained the same for all specimens. In particular, S3DP specimens were fabricated using combinations of two recoating speeds, $v_{\mathrm{r}} = 0.13$ and 0.26 m/s, and two binder contents, $b = 3.8$ and 7.2 wt% of sand (Table 2). Further material and 3D-printer specifications are given in Table 1. All four compositions show porosities close to 45%, calculated using the measured sample weight and volume. This porosity is close to the maximum porosity of 48 %, which corresponds to the loosest possible packing of spherical grains with uniform diameter and no binder. Note that we assumed a silica sand density $\rho_{\mathrm{s}} = 2.65$ g/cm^2 and a binder density $\rho_{\mathrm{b}} = 1.15$ g/cm^2 (Mitra et al., 2018) for the porosity calculation.

Table 2. Compositions for sand printing, representing different combinations of binder content b and recoating speed v_{r}. The resulting average porosity ϕ and its standard deviation (SD) are given.

Composition	b [wt% of sand]	v_{r} [m/s]	ϕ [%]	SD [%]
R1	3.8	0.13	43.7	0.6
R2	3.8	0.26	47.6	1.0
R3	7.2	0.13	42.8	4.2
R4	7.2	0.26	45.1	2.2

3 Sand-based 3D-printed material characterization

To characterize the basic mechanical and frictional properties of the S3DP material, we carried out: a) unconfined compression test on cylindrical S3DP specimens and b) shear tests on flat S3DP interfaces. The four different material compositions (Table 2) were tested, in order to analyse the effect of binder content and recoating speed on the mechanical parameters, and to choose the most suitable composition for analogue faults.

3.1 Unconfined compression tests

For the unconfined compression test, we used a uniaxial compression frame, which is equipped with a 20 kN loadcell mounted on a servo-mechanical piston. The loading for the following experiments was carried out under displacement control, measured by an integrated encoder. The vertical displacement of the top of the specimen was recorded by an LVDT. Cylindrical specimens were printed with 20 mm diameter and 40 mm height. The printing direction is along the height of the cylinder.

Typical stress-strain curves of the performed UCS tests are presented in Figure 3. More specifically, we are interested in the unconfined compressive strength (UCS), the Young modulus and the post-peak behavior (ductility/brittleness). Good repeatability was reported for tests of the same material composition.

In all of our experiments, we can observe a linear loading path above an axial stress of $\sigma_1 \approx 5$ MPa, leading to a relatively brittle failure. Below that stress level, the slope of the stress-strain curve is much smaller, indicating a possible plastic compaction due to crack and/or pore closure. After failure, we detect a significant, but gradual softening in the post-peak regime, which can be beneficial in some applications (ductility). Notice that the initial loading section of composition R1 at $\sigma_1 \approx 2$ MPa shows a distinctive plateau, which could also be due to initial misalignment of the specimen or initial local compaction of asperities at the top and bottom end surfaces.

We note that compositions R1 and R3 (low recoating speed) behave similarly, with peak stresses close to 18 MPa. Likewise, compositions R2 and R4 (high recoating speed) show similar responses, but with lower peak strengths, i.e. at around 12 MPa. The UCS strengths are summarized in Figure 4a, showing the increase of strength with lower recoating speed. Slower recoating induces higher packing density, which seems to favour mechanical strength. The binder content has negligible influence on the compressive strength.

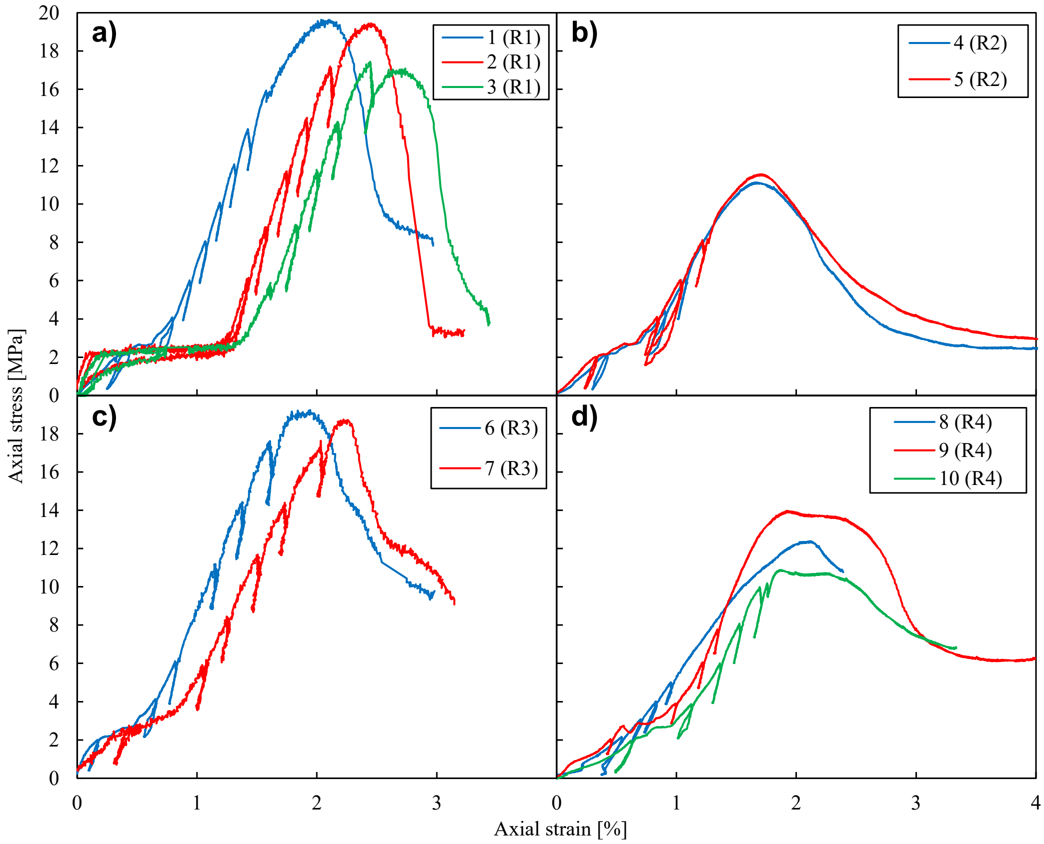

Figure 3. Experimental stress-strain behavior obtained from uniaxial compression tests on specimens with different compositions (Table 2).

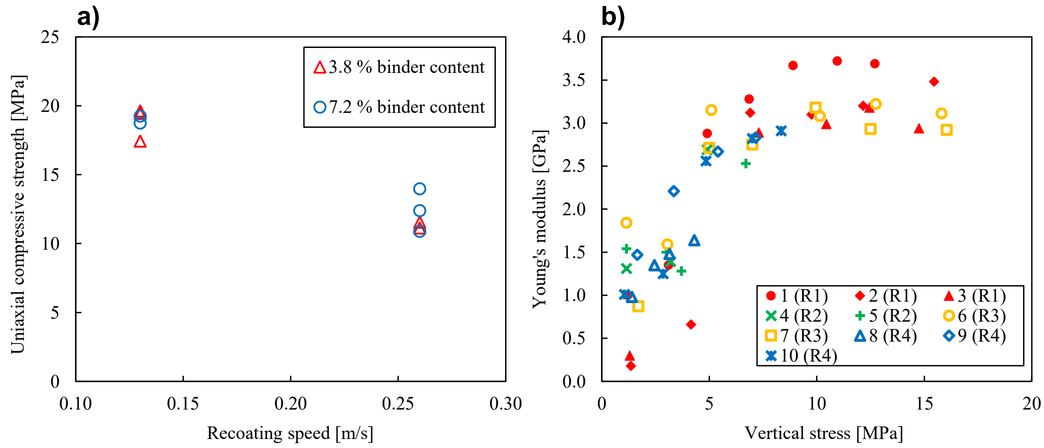

Figure 4. a) Influence of the recoating speed on the unconfined compressive strength. Different binder contents (Table 2) have no significant effect. b) Young's modulus evaluated at unloading-reloading cycles at different axial stress levels.

During the loading paths, unloading-reloading cycles were carried out to measure the elastic Young modulus E. This parameter was evaluated through linear regression on the stress-strain curve of each cycle. In Figure 4b, we plot the Young modulus with respect to the vertical stress at the beginning of the respective cycle. While the composition of the specimens does not notably affect the Young modulus E, the vertical stress has a significant impact on the stiffness. Even though we detect a rather large dispersion of values, we can observe an increase of the Young modulus with vertical stress. At $\sigma_1 = 2$ MPa, we measured $E \approx 1.0$ GPa, which increases up to $E \approx 3.3$ GPa at $\sigma_1 =$ 6 MPa. For higher stresses, the Young modulus remains practically constant.

Before each unloading-reloading cycle, the displacement was stopped for a certain time, which allowed us to measure the vertical stress relaxation. The decrease of vertical stress, starting from the initial value $\Delta\sigma_1 = \sigma_1 - \sigma_{1,0}$, was analysed relative to the initial stress $\sigma_{1,0}$, giving the dimensionless relative relaxation. Figure 5a shows a typical result of the relative relaxation with respect to time, measured on different stages for specimen 1 (composition R1). After a time of 30 s, we observe a linear behavior with respect to log-time. The relaxation coefficient c_{R} can be evaluated from the slope of the curve and its values are presented in Figure 5b in function of the normalized vertical stress (initial vertical stress over compressive strength). Independently of the sample composition, we find values of c_{R} varying between 0.010 and 0.017 s^{-1} at a vertical stress below 80 % of the compressive strength, while above that stress level, c_{R} increases up to 0.024 s^{-1} at 100 % compressive strength.

In terms of compressive strength, we found a range of values between 10 and 20 MPa, similar to the values obtained by Gomez et al. (2019) on a similar material. The observed values for compressive strength and Young's modulus are comparable to those of weak sandstones (porosity of approximately 25 %) (Dobereiner & Freitas, 1986; Papamichos et al., 2000). Interestingly, we can observe an evolution of Young's modulus with vertical stress, such as in natural sandstones (e.g. Pimienta et al., 2015). This behavior is often explained through the closure of micro-cracks, which increases the grain-to-grain contact area and consequently the stiffness.

Note that the Young modulus, the peak strength and the relaxation characteristics were determined in this study always for a loading direction perpendicular to the printing layer. For loading parallel to the layer, one can expect different properties due

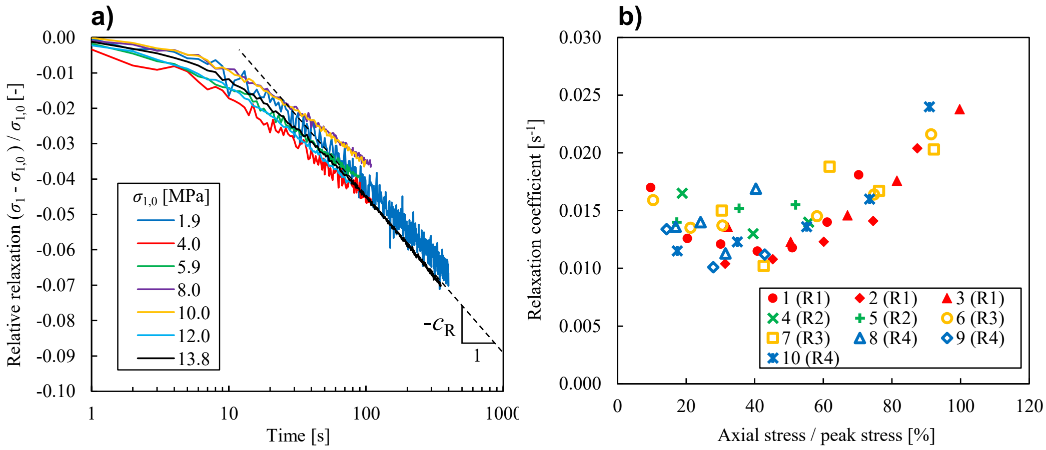

Figure 5. a) Relaxation coefficient c_{R} evaluated at constant displacement stages under different stress levels. The indicated slope provides an estimation of the relaxation coefficient c_{R}. b) Relative relaxation with respect to time under various initial axial stress levels $\sigma_{1,0}$.

to the anisotropic micro-structure of the material, but this exceeds the scope of the current work. For instance, Gomez (2017) showed for a similar S3DP material, that under loading parallel to the printing layer with respect to perpendicular loading, the strength decreased from 17.1 to 14.4 MPa, the failure characteristics changed from ductile to brittle and the Poisson ratio increased from 0.19 to 0.25, while the Young modulus remained at 1.7 GPa.

3.2 Direct shear experiments on flat interfaces

For direct shear experiments, we used the direct shear device shown in Figure 6a, which is designed for specimens composed of two blocks. The bottom one has dimensions equal to 140x100x10 mm^3 and the top one equal to 100x100x25 mm^3 (length x width x height). These blocks were printed with their height axis perpendicular to the printing layer. The length of the bottom block is higher than the one of the top block, in order to assure constant contact area (100x100 mm^2) during shearing. In the vertical direction, the controlled normal force F_{n} results in a normal stress σ_{n}, which is quasi-uniform over the interface (Tzortzopoulos et al., 2019). The vertical displacement was measured by an integrated LVDT. In the horizontal direction, a ram permits to move the lower part of the device. This is either force controlled (F_{h}) or displacement controlled (δ). The horizontal displacement induces a shear stress τ_{n}, which is considered to be uniformly distributed over the interface.

For each material composition R1 - R4, we tested two specimens under a normal stress of 500 kPa. Two additional specimens of composition R1 were sheared under 100 kPa normal stress. The apparent friction coefficient, presented for some typical results in Figure 6b, reached a constant residual plateau for the investigated shear displacement up to 6 mm. We observe a perfectly plastic behavior without any softening. Moreover, the experiments show a good repeatability. The average values of this residual friction coefficient under 500 kPa normal stress are 0.58 for R1, 0.60 for R2 and 0.63 for R3 and R4. Decreasing the normal stress in tests on composition R1 did not change the apparent friction coefficient, confirming Coulomb's assumption of proportionality.

The measurements from the direct shear tests were verified through additional friction tests on composition R1, using an inclined plane configuration (Figure 6c). In these verification tests, specimens consisting of lower and upper blocks with flat interfaces (equiv-

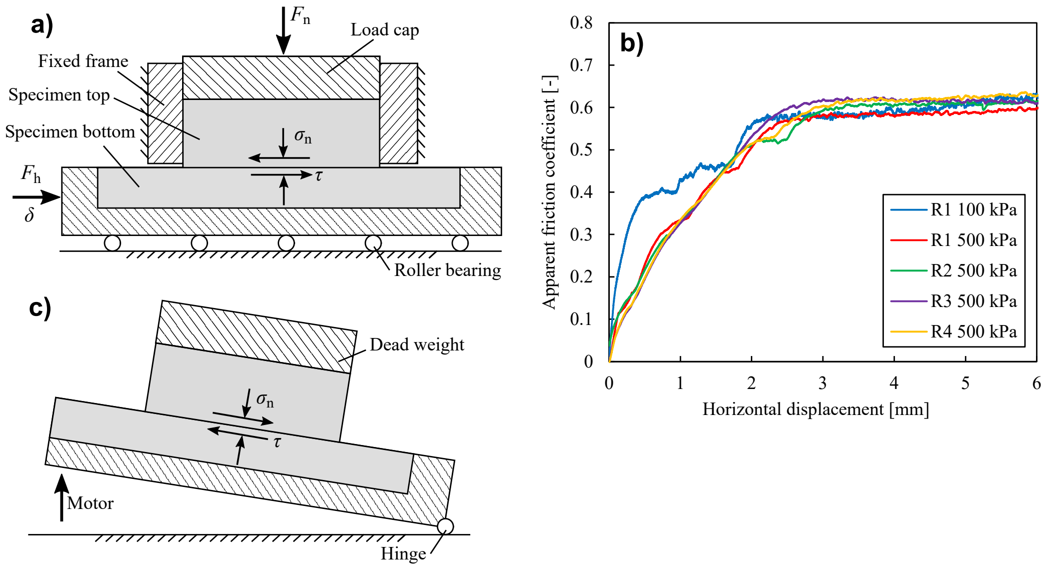

Figure 6. a) Schematic plan of the direct shear apparatus. The normal force F_n and either the horizontal force F_h or the horizontal displacement δ are controlled. b) Evolution of the apparent friction coefficient shown on one representative result for each material composition and normal stress level. c) Configuration of the inclined plane shear test.

alent dimensions as the specimens used for direct shear tests), were placed on a horizontal metal plate. The lower block was prevented from sliding on the plate, while the upper block was unconstrained. An additional weight of 1.0 kg was placed on top of the upper block. The plate was slowly inclined, until the upper block started to slide. By measuring the inclination angle, the friction coefficient of the interface could be determined. We carried out four tests in this way, showing an average friction coefficient $\mu = 0.62$ (corresponding to a friction angle of 31.8°) with a standard deviation of 5.0 %. This friction coefficient is close to the value of 0.58 obtained on the R1 composition using the direct shear apparatus, which confirms the results of the more complex device.

4 Design of interfaces with controlled friction

Once the basic mechanical properties of the sand printed material are identified, it is possible to design the geometry of the printed interfaces, in order to give them the desired frictional properties. These properties include the peak friction, the residual friction, and the characteristic slip distance. Moreover, we can control the exact evolution of friction with slip, giving us important flexibility in experiments.

4.1 Joint friction model

Modelling the frictional behavior allows us to better understand the underlying physical mechanisms and enables us a to design interfaces of desired frictional properties. According to Newland and Allely (1957); Patton (1966), and assuming Coulomb friction, the friction coefficient of rock joints is:

$$\mu = \frac{\tau}{\sigma_\mathrm{n}} = \tan(\phi_\mathrm{b} + i) \tag{1}$$

where ϕ_b is called basic friction angle and i effective roughness, or i-value in the case of rock joints (Barton, 1973). The effective roughness is the inclination of asperities along the interface.

According to Barton (1973), the value of ϕ_b corresponds to the residual friction angle, measured on saturated, planar rough-sawn or sand-blasted surfaces of the rock. This author has summarized literature data for sand-blasted and sawn surfaces, showing that most rocks have basic friction angles of approximately between 25° and 35°. The measured basic friction of the sand-based 3D printed material was found in the same range (around 30°, see Section 3.2), which makes it a good candidate for a rock analogue, as far as it concerns frictional properties.

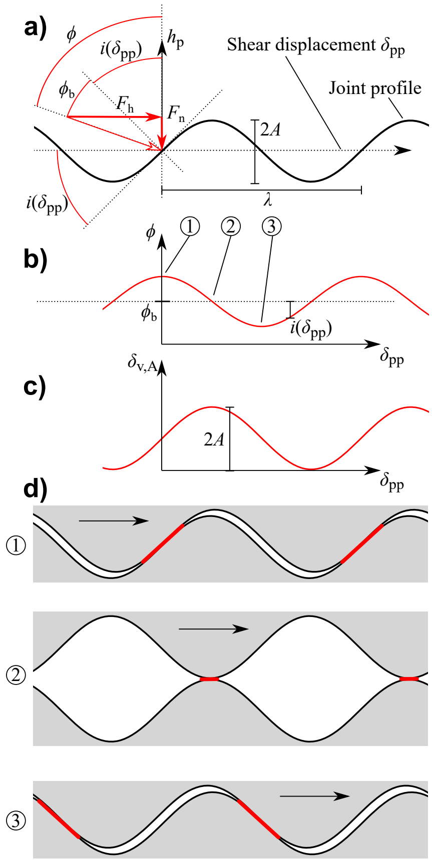

Figure 7. Friction model for a joint with periodic asperity geometry, illustrated using a sine-wave profile. a) Force diagram on the position $\delta_{pp} = 0$, where the asperity inclination i is highest. The apparent total friction angle, which gives the relationship between F_h and F_n, is the sum of i and ϕ_b. b) Oscillation of the total friction angle ϕ around the basic friction angle ϕ_b with amplitude i, depending on the shear displacement. c) Vertical displacement of the top interface. d) Asperity contact orientation (red in online version), which changes with progressing displacement and affects the total friction. Wear and compaction is neglected in this schema, so that the interface geometry remains unchanged ($A = A_0$).

By appropriately designing i in terms of slip, one can control the evolution of the apparent friction coefficient μ. In this way it is possible to imitate a great variate of frictional behavior in experiments. In order to demonstrate this idea, we apply Patton's friction relation (Eq. (1)) for periodic sine-wave asperities. This roughness profile is expressed as a function of the shear displacement δ, defined by an amplitude A_0 and a wavelength λ. In Figure 7, we present the geometry of the sinusoidal asperities. According to Eq. (1), the maximum friction is expected at the maximum profile angle i, where we set $\delta_{\mathrm{pp}} = 0$. The profile height, h_{p}, can be expressed as a function of the shear displacement δ_{pp}, resulting in $h_{\mathrm{p}}(\delta_{\mathrm{pp}}) = A_0 \sin(2\delta_{\mathrm{pp}}\pi/\lambda)$. The asperity inclination gives us the asperity friction coefficient μ_{A}, obtained through differentiation of h_{p} with respect to δ_{pp}:

$$\mu_{\mathrm{A}}(\delta_{\mathrm{pp}}) = \tan\left[i(\delta_{\mathrm{pp}})\right] = \frac{\mathrm{d}h_p(\delta_{\mathrm{pp}})}{\mathrm{d}\delta_{\mathrm{pp}}} = 2\pi\frac{A_0}{\lambda}\cos\left(2\pi\frac{\delta_{\mathrm{pp}}}{\lambda}\right) \tag{2}$$

where the maximum and minimum asperity friction μ_{A} are given by $\pm 2\pi A_0/\lambda$. Inserting Eq. (2) in (1), one can calculate the total apparent friction coefficient:

$$\mu(\delta_{\mathrm{pp}}) = \frac{\mu_{\mathrm{b}} + \mu_{\mathrm{A}}(\delta_{\mathrm{pp}})}{1 - \mu_{\mathrm{b}}\mu_{\mathrm{A}}(\delta_{\mathrm{pp}})} \tag{3}$$

where $\mu_{\mathrm{b}} = \tan\phi_{\mathrm{b}}$ is the basic friction coefficient.

In addition, the oscillating vertical compaction-dilation $\delta_{\mathrm{v,A}}$ due to the sliding over asperities (Figure 7) can be derived from the profile height $h_{\mathrm{p}}(\delta_{\mathrm{pp}}) = A_0 \sin(2\pi\delta_{\mathrm{pp}}/\lambda)$. Therefore, dilatancy can be designed as well, which, for the sinusoidal asperities, is equal to:

$$\delta_{\mathrm{v,A}}(\delta_{\mathrm{pp}}) = A_0\left[1 + \sin\left(2\pi\frac{\delta_{\mathrm{pp}}}{\lambda}\right)\right] \tag{4}$$

4.2 Wear and gouge formation

In our friction model, we intend to take into account the wear of asperities and the formation of gouge, due to the detachment of grains from the S3DP matrix (Figure 8). Note that this gouge formation could mimic the creation of gouges in real faults (Marone & Scholz, 1989; Marone et al., 1990; Rattez et al., 2018a, 2018b).

Queener et al. (1965) proposed a general law for wear, composed of an exponential transient and a linear steady-state wear, which is compatible with wear observations in rock joint shear experiments (Power et al., 1988).

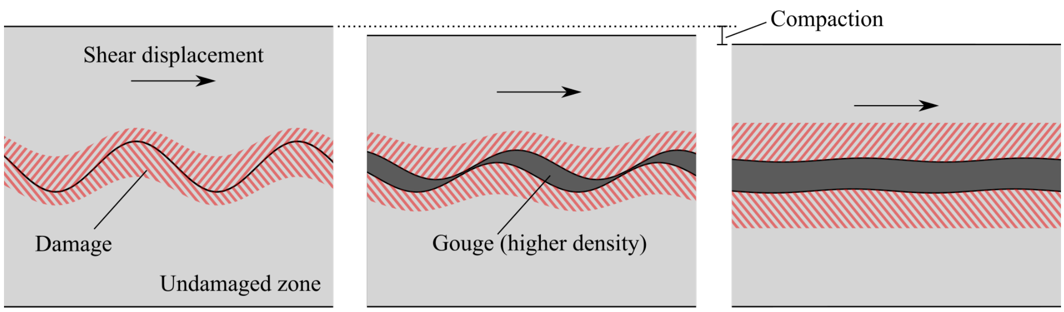

Figure 8. Schematic hypothetical representation of gradual wear of asperities. Abraded grains form a gouge layer between the interfaces. Total compaction can be due to the compaction in the damage zone and in the gouge layer.

Abrasion gradually reduces the asperity amplitude (Li et al., 2016) (Figure 8) and therefore the asperity friction affected by wear is denoted by $\mu^*_{\mathrm{A}}(\delta_{\mathrm{pp}})$. For very large displacements, $\mu_{\mathrm{A}}(\delta_{\mathrm{pp}})$ becomes zero and $\mu = \mu_{\mathrm{b}}$ (Eq. (3)). We consider here exponential abrasion, which reduces the apparent asperity friction coefficient $\mu^*_{\mathrm{A}}(\delta_{\mathrm{pp}})$:

$$\mu(\delta_{\mathrm{pp}}) = \frac{\mu_b + \mu_{\mathrm{A}}^*(\delta_{\mathrm{pp}})}{1 - \mu_{\mathrm{b}}\mu_{\mathrm{A}}^*(\delta_{\mathrm{pp}})} \tag{5}$$

$$\mu_{\mathrm{A}}^*(\delta_{\mathrm{pp}}) = \mu_{\mathrm{A}}(\delta_{\mathrm{pp}})\, e^{-c_{\mathrm{w}}\delta_{\mathrm{pp}}} \tag{6}$$

The frictional behavior of this designed interface can therefore be adjusted through two asperity properties and two material parameters. These parameters are the wavelength λ, which governs the period in which the friction oscillates, and the amplitude A_0, which defines the asperity friction. Moreover, the material composition affects the basic friction μ_{b} and the wear coefficient c_{w}.

In terms of vertical displacement, the maximum compaction $\delta_{\mathrm{v,max}}(\delta)$ is a function of the total shear displacement δ and can be described by an empirical exponential law (Power et al., 1988):

$$\delta_{\mathrm{v,max}}(\delta) = \delta_{\mathrm{v},\infty}\left(1 - e^{-c_{\mathrm{v}}\delta}\right) \tag{7}$$

where c_{v} is the vertical compaction coefficient and $\delta_{\mathrm{v},\infty}$ the final steady state compaction.

Moreover, we can superpose the oscillating vertical compaction-dilation $\delta_{\mathrm{v,A}}$ due to the sliding over asperities (Eq. (4), see also Figure 7) to Eq. (7). As described above (Eq. (6)), the amplitude of the asperities decreases due to wear, governed by the wear coefficient c_{w}. The asperity dilation accounting for wear is then written as:

$$\delta_{\mathrm{v,A}}^*(\delta_{\mathrm{pp}}) = A_0\, e^{(-c_{\mathrm{w}}\delta_{\mathrm{pp}})}\left[1 + \sin\left(\delta_{\mathrm{pp}}\frac{2\pi}{\lambda}\right)\right] \tag{8}$$

The total vertical displacement is the sum of compaction and asperity dilation:

$$\delta_{\mathrm{v}}(\delta_{\mathrm{pp}}) = \delta_{\mathrm{v,max}}(\delta) + \delta_{\mathrm{v,A}}^*(\delta_{\mathrm{pp}}), \quad \delta = \delta_{\mathrm{pp}} + \delta_1 \tag{9}$$

where δ_1 is the total shear displacement at the first peak of the apparent friction coefficient. Power et al. (1988) stated that in laboratory shear tests, most of the wear occurs in the "transient wear phase". Laboratory specimens have a finite roughness scale, and most of that initial roughness is destroyed during the initial, transient wear phase. Moreover, created gouge material often isolates the bare rock interfaces and reduces the apparent friction (Figure 8). According to these authors, this first transient wear is followed by steady-state wear, which continues in laboratory tests under a relatively slow rate, as most of the asperities are flattened out. In real faults however, fault roughness is self-affine and covers a much larger range of scales (e.g. Schmittbuhl et al., 1993; Candela et al., 2012). As a result, the size of the asperities that must be broken increases approximately linearly with displacement. Hence, real faults never reach a steady state wear as experimental faults do (Power et al., 1988). In our experiments, we investigate a finite roughness scale, equal to the size of the sine-waves. Steady state wear is therefore expected to be negligible and not considered in the model.

4.3 Direct shear experiments with designed roughness

Direct shear experiments were performed on S3DP material with controlled roughness properties, to study the effectiveness of our theoretical friction design approach. For this purpose, we printed sine-wave interface asperities with a constant amplitude $A = 3D_{50} = 0.42$ mm and constant wavelength $\lambda = 20D_{50} = 2.80$ mm, as shown in Figures 6 and 9.

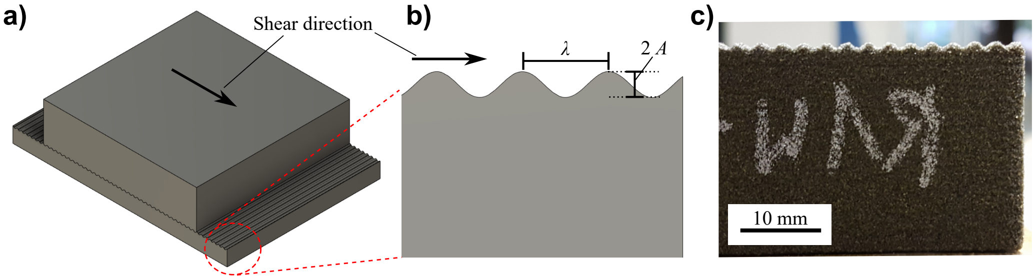

Figure 9. **a)** 3D model for printing the two direct shear specimen blocks with wave interfaces. **b)** Plan view zoom on the sine-wave interface with amplitude $A = 0.42$ mm and wavelength $\lambda = 2.80$ mm. **c)** Photograph of a printed specimen, zoomed on the interface.

A series of direct shear tests under a constant normal stress of 500 kPa was carried out on samples of the four different compositions. The specimens were initially loaded with a normal stress of 500 kPa and sheared under constant normal stress and constant displacement rate of 0.5 mm/min for 10 mm. After the maximum displacement was reached, the specimen was sheared in the reverse direction, until its initial position. In this way, a full loading cycle was performed, corresponding to a total of 20 mm of accumulated slip. Figures 10 (compositions R1 and R2) and 11 (compositions R3 and R4) present the evolution of the measured friction coefficient and the vertical displacement with progressing horizontal displacement. In particular, we show the apparent friction coefficient μ, defined as the ratio of $F_\mathrm{h}/F_\mathrm{n}$. Negative values correspond to reverse shearing. One can clearly observe oscillations in the post-peak regime of the friction behavior, due to the wave geometry of the interfaces. The interlocking printed asperities induce a much higher peak friction, close to 1.0, compared to the one measured on the flat surface, close to 0.6. Once we exceed the peak, the friction decreases and drops to a lower level than the one determined on flat specimens (negative asperity friction angle i, see Eq. (1)). Then, the friction rises and falls in the form of damped oscillations, due to wear. In terms of vertical displacement, the specimens exhibit an overall compaction during shearing, combined with dilation peaks of decreasing amplitude.

In Table 3, we present different frictional properties evaluated from the experimental results (Figure 10). The maximum friction coefficient measured at the first peak (μ_1) is shown. At the end of the reverse loading (negative apparent friction), the amplitude of friction oscillations becomes almost zero. Inspecting the specimens after the experiments confirmed that wear has flattened out the sine-wave asperities and left an almost flat interface. One can estimate the residual friction coefficient μ_∞ from the mean friction in this part of the experimental curve, which results in being almost identical to μ_b (asymptotical approximation for infinite sliding). In theory, differences may arise due to a higher amount of gouge material present when evaluating μ_∞. Comparing the values of μ_∞ with the results from flat interface shear experiments, no significant difference can be observed. The wavelengths λ_1 and λ_2 are the slip distances between two points of maximum and minimum friction, respectively. Their average value is λ, which corresponds in theory to the wavelength of the printed interface.

4.3.1 Effect of material composition

For high binder content, the recoating speed (packing density) appears to have a minor influence on the friction, as we observe similar values $\mu_1 = 0.96$ and 0.93 for R3 and R4, respectively. For low binder content, we measured $\mu_1 = 1.07$ for R1 and 0.88 for R2. According to our results, higher density induces higher friction. Moreover, for

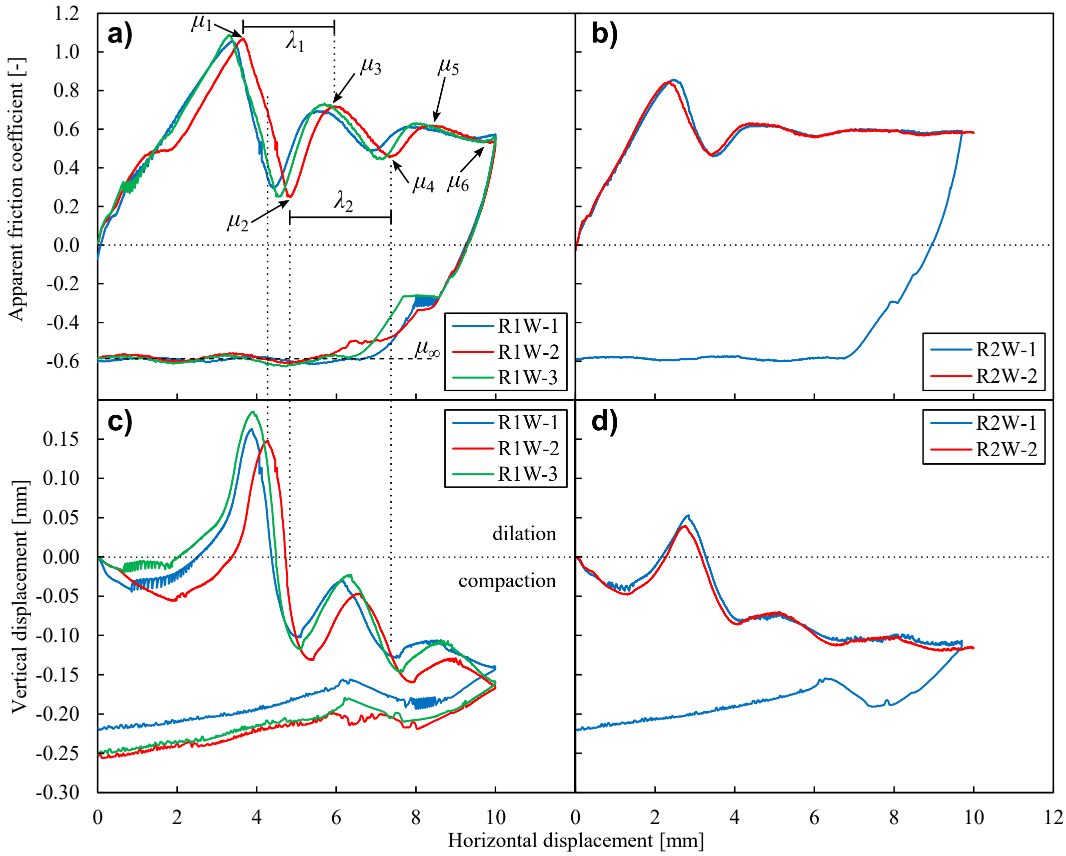

Figure 10. Results of direct shear experiments under 500 kPa normal stress on specimens R1 and R2 (Table 3). a), b) Friction coefficient and c), d) vertical displacement with respect to horizontal shear displacement. Note that due to technical problems, the reverse shearing of R2W-2 was not carried out.

high density, the friction is higher under low binder content. This is probably due to a higher possibility for grains to interlock in the absence of binder. The friction for large shear displacement μ_∞ does not appear to be significantly influenced by the material composition, providing values close to 0.6 (Table 3), which is equal to μ_b measured on flat specimens in Section 3.2.

Regarding the average wavelength λ, we cannot see any clear influence of the material composition. These values are close to the designed geometric wavelength of the interface $\lambda = 2.40$ mm. Note that the vertical displacement shows the same wavelength, but, as expected, here the oscillations are shifted by $\approx \lambda/4$. This evidences that the behavior of vertical displacement is correlated with the asperity profile. In other words, the friction coefficient reaches its local extrema when the inclination of asperities (the slope of the vertical displacement over horizontal displacement) also has a local extremum (Figures 10 and 11).

The decrease of the friction amplitude differs between the compositions due to wear. For the R1 and R2 specimens (low binder content) the reduction of the amplitude is more prominent (Figure 10), and we observe a nearly constant friction at the end of the first loading phase and during the reverse loading. This residual friction coefficient corresponds to the one of a planar interface, due to complete abrasion of the asperities. This friction reduction can be approximated with an exponential law (Eq. (6)). Rewriting Eqs. (6)

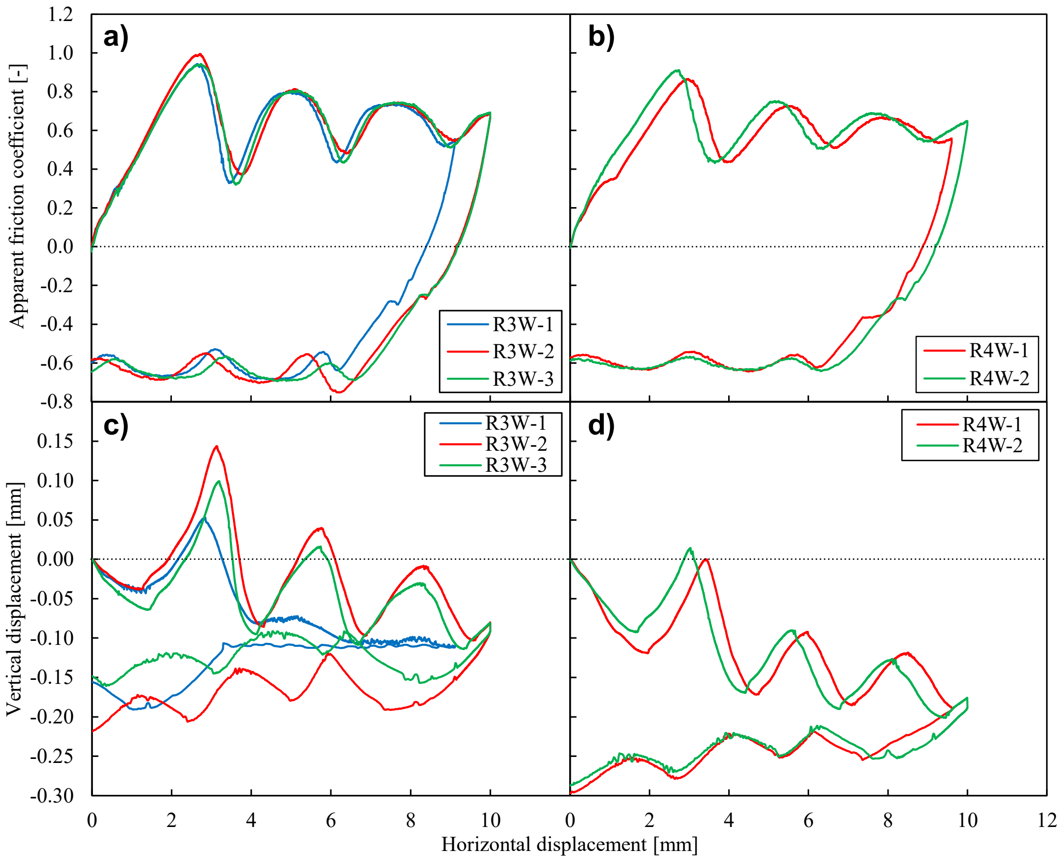

Figure 11. Results of direct shear experiments under 500 kPa normal stress on specimens R3 and R4 (Table 3). a), b) Friction coefficient and c), d) vertical displacement with respect to horizontal shear displacement.

and (5), we can determine the relative asperity friction R, which is initially equal to 1.0 and decreases to zero for progressing wear:

$$R = e^{-c_{\mathrm{w}}\delta_{\mathrm{pp}}} = \frac{(|\mu_i - \mu_\infty|)(1 + \mu_1\mu_\infty)}{(\mu_1 - \mu_\infty)(1 + \mu_i\mu_\infty)} \tag{10}$$

The relative asperity friction is plotted for a typical experiment (R1W-1) in Figure 12, on which we can obtain the wear coefficient c_{w} through least square fitting (Table 3).

We observe a stronger dependency of the wear characteristics on binder content than on recoating speed. Compositions with a binder content $b = 3.8\%$ show c_{w} between approximately 0.4 and 0.6, while for $b = 7.2$, we measured c_{w} between approximately 0.2 and 0.4. Increasing the recoating speed, from 0.13 to 0.26 m/s, the average value of c_{w} increases for about 0.1.

Evaluating the local minima $\delta_{\mathrm{v},i}$ of the vertical displacement evolution δ_{v}, one observes a general compaction, which starts immediately at $\delta = 0$, before the first friction peak. For large δ, the curves appear to approach a constant vertical displacement $\delta_{\mathrm{v},\infty}$ (c.f. critical state, e.g. Wood, 1991). This global compaction is represented by the exponential law (Eq. (7)). Equation (7) can be rewritten, to introduce the relative com-

Table 3. Mean values of the parameters determined from the direct shear tests under σ_n = 500 kPa on wave interfaces (see also Figures 10 and 11), and their standard deviation (SD). The amplitude A_0 is back-calculated using Eq. (12).

	μ_1		λ		δ_1		μ_∞		c_w		$\delta_{v,\infty}$		c_v		A_0
	mean	SD	mean	SD	mean	SD	mean	SD	mean	SD	mean	SD	mean	SD	
	[-]	[%]	[mm]	[%]	[mm]	[%]	[-]	[%]	[-]	[%]	[-]	[%]	[-]	[%]	[mm]
R1	1.07	1.8	2.41	4.4	3.45	5.4	0.57	2.0	0.45	26.0	-0.18	5.6	0.21	8.9	0.118
R2	0.85	0.8	2.45	2.0	2.41	2.9	0.58	1.2	0.60	4.7	-0.12	10.5	0.36	29.9	0.071
R3	0.96	3.2	2.55	0.8	2.71	2.0	0.61	1.9	0.19	12.7	-0.11	4.6	0.42	21.3	0.091
R4	0.89	3.6	2.54	1.1	2.86	5.7	0.60	1.2	0.26	0.8	-0.20	7.1	0.43	29.5	0.078

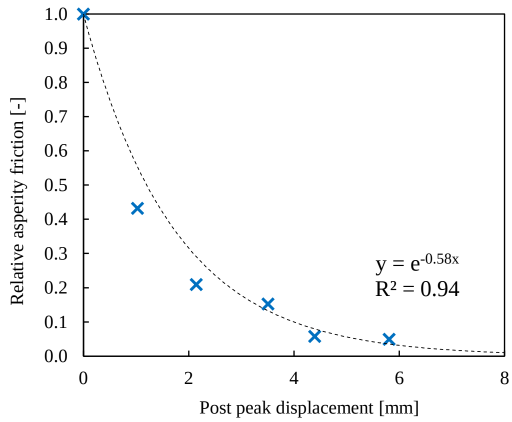

Figure 12. Decrease of relative asperity friction with progressing displacement and wear on a typical wave interface shear test (R1W-1). The wear coefficient c_w can be evaluated using an exponential fit.

paction R_v, which can be evaluated at the local peaks of vertical displacement:

$$R_v = e^{-c_v \delta} = 1 - \frac{\delta_{v,i}}{\delta_{v,\infty}} \tag{11}$$

The relative compaction values, determined on a typical experiment, are presented in Figure 13. One can obtain the values of c_v and $\delta_{v,\infty}$ by a least square error fit. This relationship captures only the overall vertical compaction, while in the experiments, we also observe significant oscillations due to asperities. In the following section, we are able to model these peaks of vertical displacement using Eqs. (7) - (9) with previously evaluated properties. Consequently, no additional model parameters are required.

4.3.2 Effect of normal stress

In order to explore the influence of the applied normal stress on shear behavior, we carried out the same shear experiments under 100 kPa normal stress on specimens made of composition R1 (Figure 14, Table 4). The most important change of behavior is observed on the wear, presented in terms of the wear coefficient c_w in Figure 15a. Otherwise, Coulomb's assumption of proportionality is valid. By reducing the normal stress, the decay of the friction oscillation is strongly reduced, giving a lower wear coefficient. Due to the lower normal stress, local stresses at the asperities decrease, resulting in less breakage/chipping of the asperities. This becomes also clear on the measured after the

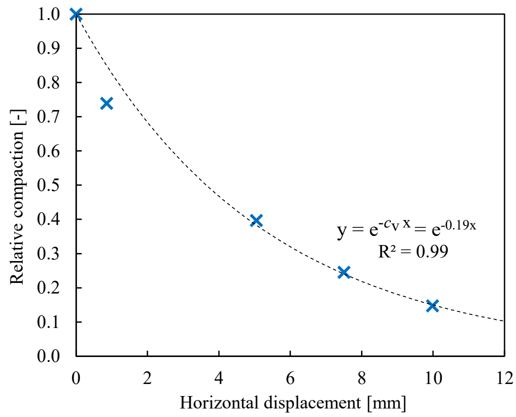

Figure 13. Measured relative vertical compaction on a typical wave shear experiment (R1W-1). The compaction is modelled through an exponential law, where the wear coefficient c_v can be evaluated using an exponential fit.

463 tests, which was almost two times higher for test under 500 kPa normal stress (average
464 loss of 1.7 g under 100 kPa and 3.2 g under 500 kPa).

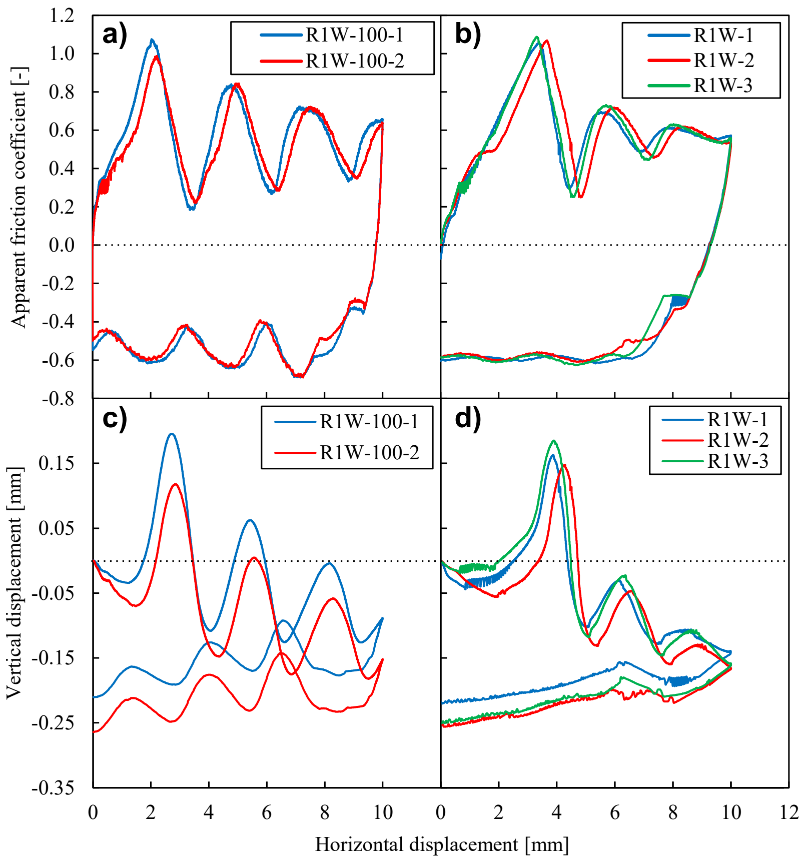

Figure 14. Friction experiments carried out on composition R1 under different normal stress of: a), c) 100 kPa and b), d) 500 kPa.

Table 4. Parameters determined from direct shear tests on wave interfaces of composition R1 under different normal stress (see also Figures 10 and 14). The respective standard deviations are denoted by SD. The amplitude A_0 is back-calculated using Eq. (12).

σ_n	μ_1		λ		δ_1		μ_∞		c_w		$\delta_{v,\infty}$		c_v		A_0
	mean	SD	mean	SD	mean	SD	mean	SD	mean	SD	mean	SD	mean	SD	
[kPa]	[-]	[%]	[mm]	[%]	[mm]	[%]	[-]	[%]	[-]	[%]	[-]	[%]	[-]	[%]	[mm]
500	1.07	1.8	2.41	4.4	3.45	5.4	0.57	2.0	0.45	26.0	-0.18	5.6	0.21	8.9	0.118
100	1.03	6.0	2.67	1.6	2.13	6.1	0.50	2.8	0.14	17.1	-0.16	24.7	0.40	2.6	0.149

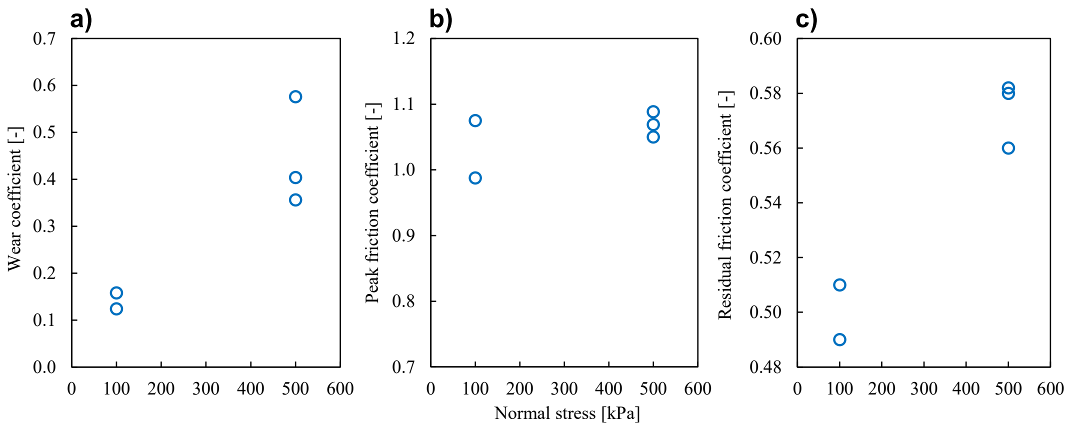

Figure 15. Effect of normal stress on the friction characteristics: a) Wear coefficient, b) first peak friction and c) final friction of the abraded interface.

No effect of the normal stress on the first peak friction coefficient μ_1 was reported (Figure 15b). Conversely, the residual friction μ_∞ appears to be slightly influenced by the normal stress (Figure 15c). Higher normal stress (500 kPa) leads to higher friction ($\mu_\infty \approx 0.57$), while under 100 kPa, we recorded $\mu_\infty \approx 0.50$.

4.4 Validation of the design model

We used the parameters evaluated on the five different test configurations (four compositions, one additional normal stress level) and insert them in the model equations for calculating the apparent friction coefficient μ (Eq. (5)) and the vertical displacement δ_v (Eq. (9)) in function of the shear displacement δ. The effective amplitude A_0 is determined indirectly from the wavelength, the basic friction and the first peak friction coefficient $\mu = \mu_1$ (Eqs. (2) and (3)):

$$A_0 = \frac{\lambda(\mu_1 - \mu_b)}{2\pi(1 + \mu_1\mu_b)} \tag{12}$$

This model parameter A_0 can differ from the design amplitude A due to to the printing resolution. Besides possible printing uncertainties, asperity abrasion could also occur during transport and handling of the printed specimens. Moreover, during the mounting of specimens in the experimental devices, loose grains could deposit in the convex areas of the interface, which could prevent a complete interface contact and therefore reduce the effective amplitude from A to A_0. Given a printing resolution of 280 μm (corresponding to two grain diameters), we expect an error of the amplitude A in this range, which is quite high. Therefore, the most reliable way for estimating the amplitude A_0 for the interfaces designed herein is through Eq. (12).

Using the parameters presented in Table 3 and 4, we are able to calculate the expected friction behavior (Eq. (5)) and vertical displacement (Eq. (9)) of our laboratory experiments. The results of these calculations are presented in Figures 16 and 17 together with the experimental curves. Notice that our main focus is on modelling the behavior after the first peak of friction. Before this point, in the loading branch, one could use a linear approximation for the shear force over shear displacement response and interpolate the vertical displacement.

Our model mimics very well the measured friction behavior with its oscillations. In addition, the vertical displacement (dilatancy) can be reproduced well, requiring only the identification of the overall compaction curve (red dashed line) as additional model parameters. The additional oscillations (red solid line) are obtained from the relationships with the friction behavior, which confirm the model presented herein. As a result, this approach could be used for the design of interfaces of custom frictional properties (see Section 5).

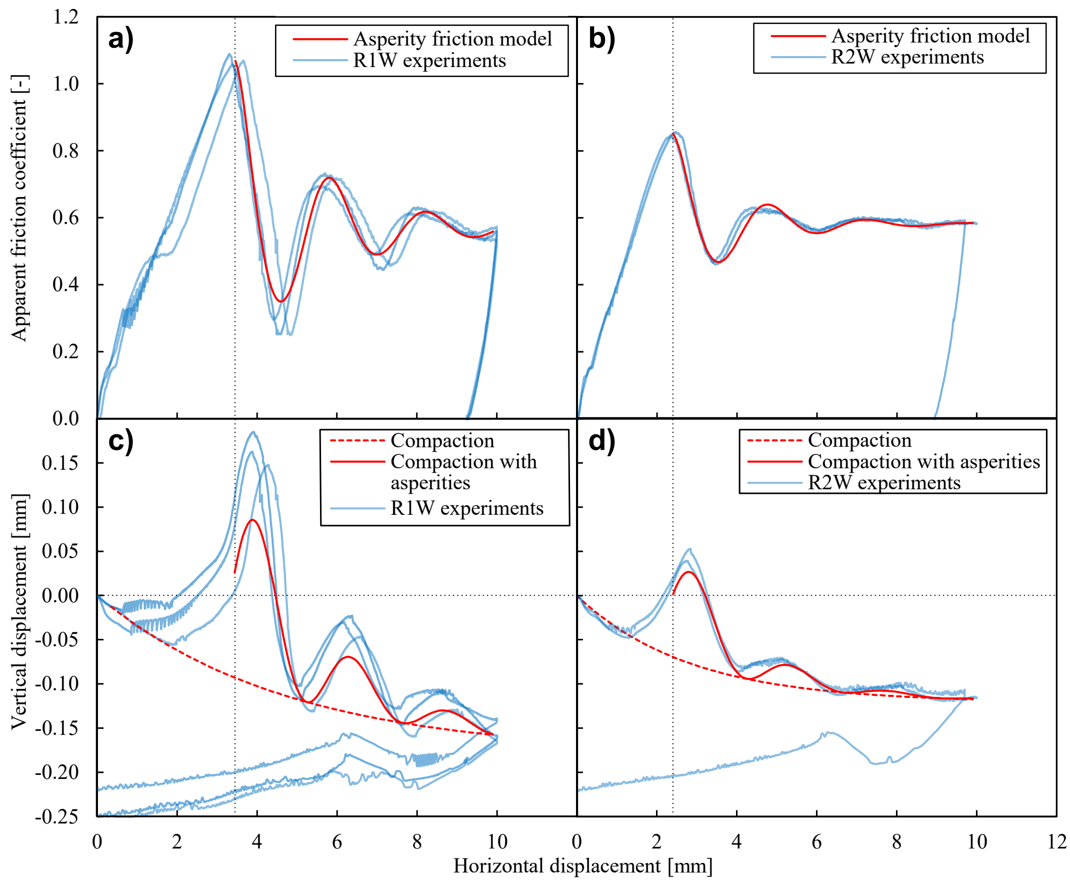

Figure 16. a), b) Evolution of friction and c), d) evolution of vertical displacement with respect to the horizontal displacement, of R1 and R2 specimens under 500 kPa normal stress. The behavior calculated by our friction model (red solid lines) is compared with the experimental data (blue solid lines).

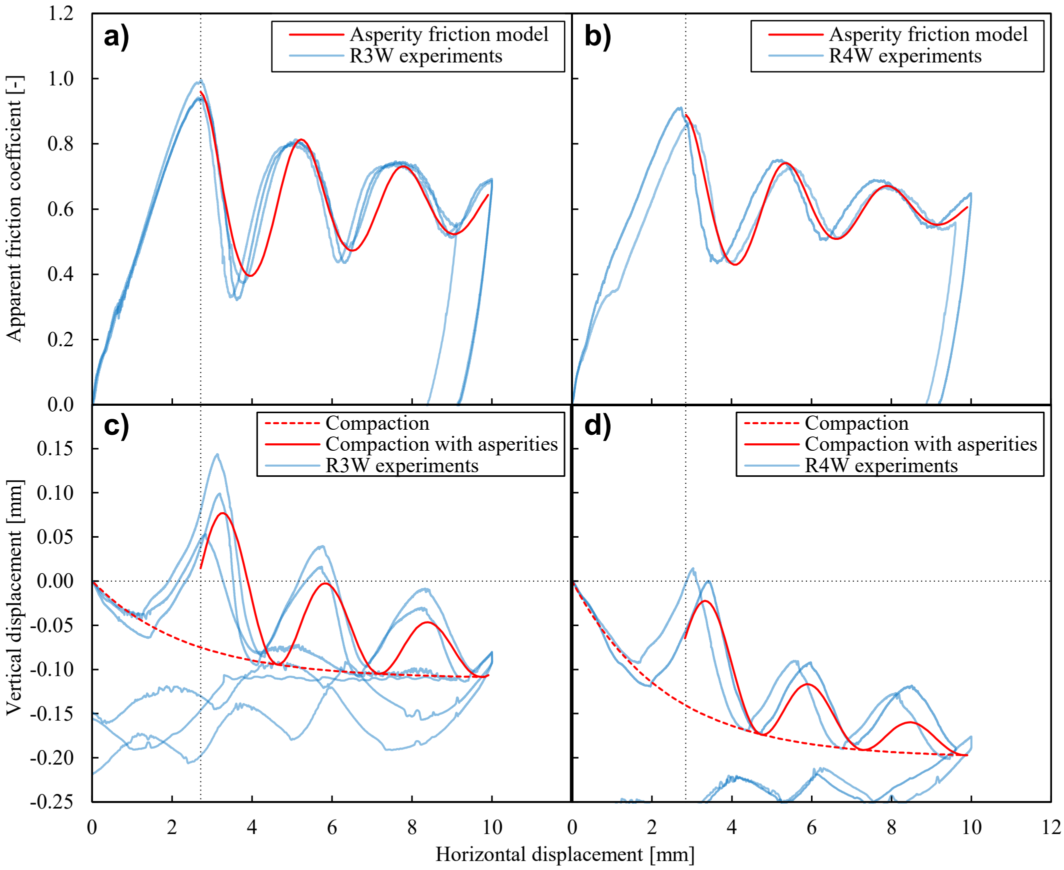

Figure 17. a), b) Evolution of friction and c), d) evolution of vertical displacement with respect to the horizontal displacement, of R3 and R4 specimens under 500 kPa normal stress. The behavior calculated by our friction model (red solid lines) is compared with the experimental data (blue solid lines).

5 Discussion

The presented experiments confirmed a good correspondence between the experimental behavior and our simple geometry-dependent friction law. The principal aspects and perspectives of this new method for creating analogue fault interfaces are presented below.

The stress drop and the characteristic slip distance govern the weakening behavior of faults. Our surrogate experiments and model show that these properties can be adjusted by tuning the geometrical properties of the 3D-printed interfaces. For sinusoidal interfaces, we confirmed both theoretically and experimentally, that the characteristic slip distance d_c is equivalent to half the asperity wavelength λ. By using Eqs. (5) and (6), one can determine the friction drop $\Delta\mu = \mu(\delta_{pp} = \lambda/2) - \mu(\delta_{pp} = 0)$, and the characteristic slip distance d_c:

$$\Delta\mu = \left(1 + e^{-c_w \lambda/2}\right)\left(1 + \mu_b^2\right)\left[\frac{\lambda}{2\pi A_0} - \mu_b\left(1 + \frac{2\pi A_0}{\lambda}\right) + e^{-c_w\lambda/2}\mu_b\left(1 - \mu_b\frac{2\pi A_0}{\lambda}\right)\right]^{-1} \tag{13}$$

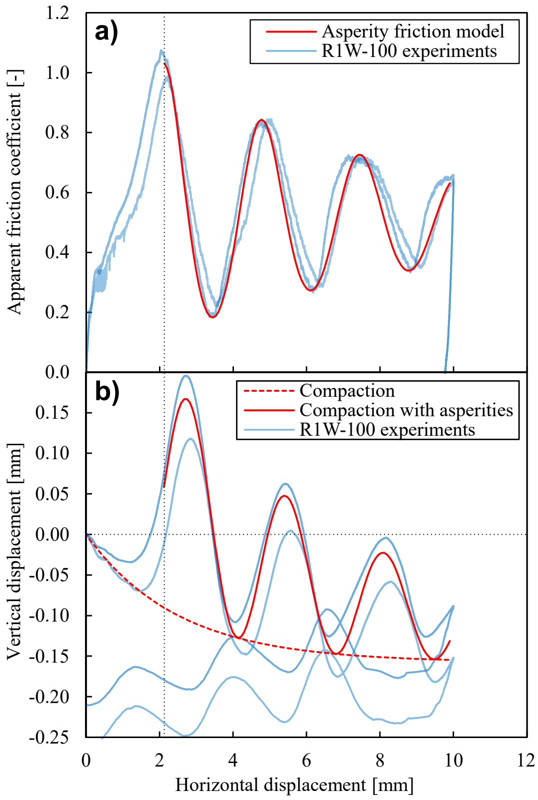

Figure 18. a) Evolution of friction and b) evolution of vertical displacement with respect to the horizontal displacement, of R1 specimens under 100 kPa normal stress. The behavior calculated by our friction model (red solid lines) is compared with the experimental data (blue solid lines).

In case of no wear, Eq. (13) simplifies to:

$$\Delta\mu = \frac{4A_0\pi}{\lambda}\,\frac{1+\mu_{\mathrm{b}}^2}{1-4\mu_{\mathrm{b}}^2A_0^2\pi^2\lambda^{-2}} \tag{14}$$

Consequently, we can obtain an approximate negative post peak slope (softening) $k_{\mathrm{pp}} = 2\Delta\mu/\lambda$. Locally, the negative post peak slope k_{pp} can be calculated through the derivative of Eq. (5). As a first approximation, if we neglect wear, this provides us a maximum of k_{pp} at $\delta_{\mathrm{pp}} = \lambda/4$, using:

$$k_{\mathrm{pp}} = -A_0\frac{4\pi^2}{\lambda^2}\left(1+\mu_{\mathrm{b}}^2\right) \tag{15}$$

This slope is important for experiments focusing on reproducing stick-slip behavior and earthquake nucleation in the laboratory (e.g. Dieterich, 1978; Tinti et al., 2016; Scuderi et al., 2017).

An interesting feature of our approach is the flexibility in the design of the frictional interfaces. For instance, here we used a sinusoidal interface, which leads to a decaying, oscillating apparent friction coefficient. These oscillations could be used for simulating sequences of healing and rupture during the seismic cycle.

Moreover, we saw that progressive sliding can reduce the friction oscillations due to the wear of asperities, accompanied by gouge creation. The applied normal stress had a significant effect on the asperity wear. Higher normal stresses increase local shear and tensile stresses, which could lead to damage of the asperities and hence reduced friction. While the material composition had a minor effect on the initial friction behavior, it played a major role in the wear and reduction of healing potential. Especially a higher binder content made the interfaces more resistant to wear. The resin binder is responsible for the material's tensile resistance and increased shear resistance, by cementing the grain-to-grain contacts. An increased binder content presumably reduces local failure of these resin-bound contacts.

In terms of dilatancy and compaction during shear, we observed a general compaction, accompanied by oscillating dilation. The dilations can be explained through the shearing over asperities which can be progressively dampened due to asperity wear. Wear is due to the failure of the bonds between the grains, which progressively leads to the flattening of the interface and to the creation of gouge material. This was evidenced by inspecting and weighting the specimens before and after shearing. The observed compaction, which seems to approach a constant value for large shear displacements, could also be explained through breaking resin bonds. In their original state, the grains in the S3DP matrix have a very loose packing. After breaking the bonds, grains are able to go into a denser packing or loosen completely in the gouge layer, causing a total volume reduction. Knowing the initial porosity (Table 2), the change in height $\delta_{\mathrm{v},\infty}$ (Table 3) and assuming a fault gouge density of 30%, we can estimate the initial height of the damage zone with values of around $6D_{50}$. Due to denser packing in gouge form, this height reduces to approximately $4D_{50}$ after transient wear. In uncemented granular soils under direct shear, shear bands develop with finite thickness, which has been observed with values around $10-18\times D_{50}$ (Roscoe, 1970; Vardoulakis & Graf, 1985; Sadrekarimi & Olson, 2010; Kozicki et al., 2013). According to Power et al. (1988), experimental faults generally show a very small wear rate, after the large scale asperities are broken, while in nature, wear progresses approximately linear with slip. These authors stated, that this difference is due to the self-similar roughness characteristics of natural faults, in contrast to the finite scale of laboratory faults. The binder content can hence be used to adjust the wear behavior of analogue faults, from high binder content providing a more constant seismic cycle, to low binder content which allows one to study progressive gouge creation (c.f. Pereira & de Freitas, 1993; Renard et al., 2012; Zhao, 2013).

When coupled with a sufficiently compliant elastic loading system, our samples can develop dynamic instabilities at the friction peaks. Potential precursors of the peaks can be investigated when looking at the shape of the friction behavior at these locations. The subsequent peaks after the first one have a fairly smooth behavior, which could help to anticipate these peaks due to $\mathrm{d}\mu/\mathrm{d}\delta \rightarrow 0$. At the first peak however, a rather sharp transition between linear loading behavior (positive slope) towards the friction behavior (negative slope) is observed. In this case, one can analyse the vertical displacement, which has a smoother behavior than the friction evolution. According to our measurements and the theoretical model without considering wear, the curvature of the vertical displacement δ_{v} (Eq. (9)) at a friction peak approaches zero ($\mathrm{d}^2\delta_{\mathrm{v}}/\mathrm{d}\delta^2 \rightarrow 0$). This behavior could be related to pressure changes in experiments, where fluids are injected into the the S3DP interface.

More generally, the frictional properties of an analogue fault interface are controlled through the maximum and minimum profile angles $i_{\max}$ and $i_{\min}$, the slip distance d_{c} and the "healing" distance d_{h} (Figure 19). The maximum and minimum angles govern the peak and minimum friction, respectively. The distance d_{c} is equivalent to the displacement between peak and minimum friction, while d_{h} defines the displacement from minimum to maximum friction. The sum $d_{\mathrm{c}}+d_{\mathrm{h}}$ denotes the total displacement between recurring friction peaks. By connecting these two points of given angles using splines, one can obtain the complete interface profile with controlled properties. Note that depending on the asperity geometry, local stresses can exceed the resistance of the material and cause wear, which flattens the asperities gradually and can create gouge material.

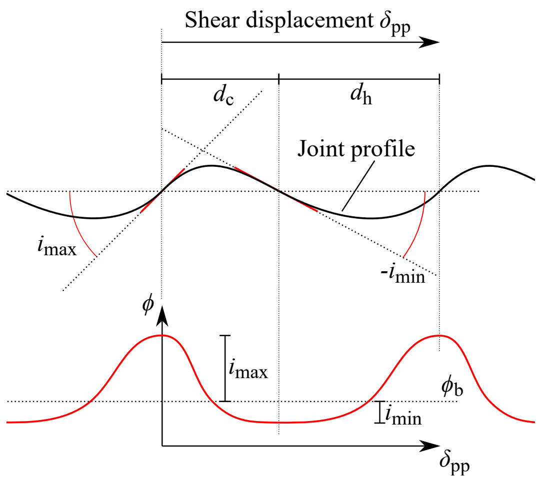

Figure 19. Schematic representation of a controlled joint friction behavior with adjustable maximum and minimum friction, slip and "healing" distance.

In this study we investigated only interfaces with one scale of asperities besides the micro-roughness. Our asperity scale was approaching the lower possible limit, due to the minimum printing resolution. Conversely, for larger asperity scales, the 3D-printing method is only limited by the printer's size, and different scales could be combined in one specimen. Moreover, we used only a 2D height profile, while one could print interfaces with 3D profiles, including for instance fault patches with different properties (Barbot et al., 2012) or in-situ roughness (Kirkpatrick et al., 2020). In addition, the permeability of the material could be adjusted through microstructure modifications (Mitra, El Mansori, et al., 2019) and printing of flow channels (Head & Vanorio, 2016), which would allow one to carry out experiments with the presence of fluid and to simulate anthropogenic injections into the fault zone.

6 Conclusions

Analogue experiments have an important role in fault mechanics, as they can help in testing various scientific hypotheses on the base of repeatable and controlled experiments. A great variety of experimental configurations has been proposed and explored in the literature (Rosenau et al., 2017). Central to those experiments is the selection of appropriate analogue, rock-like materials. Here we investigated, for the first time, the frictional properties of 3D sand-printed materials, which show a high potential for surrogate laboratory experiments involving frictional rock-like interfaces.

Pursuing further the works of Gomez (2017); Gomez et al. (2019), we first performed detailed uniaxial compression tests, in order to identify the main bulk mechanical parameters of this new material. In particular we determined the Young modulus, the compressive strength and the relaxation properties. Complete stress-strain curves were presented including the post-peak mechanical behavior of the specimens tested. Good repeatability was shown in all experiments, which allowed us to explore the role of the recoating speed and of the binder saturation during printing on the mechanical response of the samples. These two printing parameters are crucial in binder-jetting 3D printing (Gomez et al., 2019) and, besides the mechanical and frictional parameters, they can significantly influence the geometrical resolution of the printed specimens. According to our experiments, the mechanical properties of this material are close to weak sandstones (e.g. Dobereiner & Freitas, 1986; Papamichos et al., 2000).

However, the main target of this study was the investigation of the frictional properties of the sand-printed material. For this purpose direct shear tests on flat sand-printed interfaces were conducted. Two normal stress levels were considered in order to identify the apparent friction coefficient. The experimental results from the direct shear tests were corroborated with simpler inclined plane frictional tests. An apparent angle of friction of approximately 31° was determined ($\mu \approx 0.6$), which is in the range of the friction angle of many geomaterials and rock interfaces. The recoating speed and the binder saturation during printing showed to have a secondary role regarding the frictional behavior. However, these parameters did influence the creation of the thin gouge-like granular layer during shearing. Debonding of the granular particles are responsible for this thin layer, whose thickness was quantified in our experimental investigation.

The next step of our analysis was to adequately design the printed geometry of the sliding interfaces, in order to assure a desired frictional behavior. To this extend, based on the dependence of friction on roughness and using Patton's law (Patton, 1966), we presented how we can achieve desired/controlled a) maximum, minimum and residual apparent frictional properties, b) characteristic slip distance (the so called d_c), c) evolution of friction coefficient with slip and d) dilatancy. Next, we performed tests on printed interfaces of sinusoidal geometry. This geometry enabled us to verify, in a quantitative manner, the theoretical predictions of the underlying mathematical model that we derived and presented in details for designing analogue fault interfaces with this printing technique. Moreover, this periodic pattern lead to an oscillating evolution of the friction coefficient, which could be used in order to phenomenologically describe and simulate the periodical rupture and healing of fault sections. Additionally, it enhanced the creation of a gouge-like layer due to wearing of the sinusoidal peaks of the printed pattern. The thickness of this layer was also quantified and the evolution of the friction coefficient with slip was presented in details. Of course, 3D printing offers a large flexibility in creating interfaces of specific roughness and complexity.

Only sinusoidal interfaces were examined in this work, in order to present the methodology and show the potential of the technique in a simple way. The apparent frictional behavior of interfaces of more complex shapes can be estimated with the simple mathematical model presented herein. Consequently, this printing method can be exploited for the design of new surrogate experiments in fault mechanics, depending on the exact scaling laws that will be used and dictate the window of acceptable frictional parameters. For instance, by adjusting the elasticity of the tested system, earthquake triggering could be studied in the laboratory, shedding light in many open scientific questions related to induced/triggered seismicity. However, the use of this material is not limited in fault mechanics and can serve in other applications in geomechanics and geotechnics, such as tunneling, slope stability, landslides etc..

It is worth mentioning that the effect of anisotropy, Poisson ratio, rate and state behavior, porosity and fluid flow, among others, was not investigated in this work. However, the results presented herein give sufficient data for designing new analogue experiments in fault mechanics that can help in building understanding in earthquake rupture and testing new methods on seismic slip control (Stefanou, 2019).

Data Availability Statement

Data archiving is underway in https://svn.ec-nantes.fr/.

Acknowledgments

Funding: This work was supported by the European Research Council (ERC) under the European Union Horizon 2020 research and innovation program (Grant agreement no. 757848 CoQuake), *http://coquake.com*.

Contribution: All authors contributed to the analysis and writing the manuscript.

Competing interests: The authors declare that they have no competing interests.

References

Anthony, J. L., & Marone, C. (2005). Influence of particle characteristics on granular friction. *Journal of Geophysical Research*, *110*(B08409), 1–14. doi: 10.1029/2004JB003399

Asadi, M. S., Rasouli, V., & Barla, G. (2013). A Laboratory Shear Cell Used for Simulation of Shear Strength and Asperity Degradation of Rough Rock Fractures. *Rock Mechanics and Rock Engineering*, *46*(4), 683–699. doi: 10.1007/s00603-012-0322-2

Barbot, S., Lapusta, N., & Avouac, J.-P. (2012). Under the Hood of the Earthquake Machine : Toward Predictive Modeling. *Science*, *336*(6082), 707–710. doi: 10.1126/science.1218796

Barton, N. (1973). Review of a new shear-strength criterion for rock joints. *Engineering Geology*, *7*(4), 287 - 332. Retrieved from `http://www.sciencedirect.com/science/article/pii/0013795273900136` doi: https://doi.org/10.1016/0013-7952(73)90013-6

Bommer, J. J., Oates, S., Cepeda, J. M., Lindholm, C., Bird, J., Torres, R., … Rivas, J. (2006). Control of hazard due to seismicity induced by a hot fractured rock geothermal project. *Engineering Geology*, *83*(4), 287 - 306. Retrieved from `http://www.sciencedirect.com/science/article/pii/S0013795205003108` doi: https://doi.org/10.1016/j.enggeo.2005.11.002

Brace, W. F., & Byerlee, J. D. (1966). Stick-slip as a mechanism for earthquakes. *Science*, *153*(3739), 990–992. Retrieved from `https://science.sciencemag.org/content/153/3739/990` doi: 10.1126/science.153.3739.990

Brune, J. N. (1973). Earthquake modelling by stick-slip along precut surfaces in stressed foam rubber. *Bulletin of the Seismological Society of America*, *63*(6), 2105–2119. doi: 10.1016/0148-9062(74)90186-7

Candela, T., Renard, F., Klinger, Y., Mair, K., Schmittbuhl, J., & Brodsky, E. E. (2012). Roughness of fault surfaces over nine decades of length scales. *Journal of Geophysical Research: Solid Earth*, *117*(8), 1–30. doi: 10.1029/2011JB009041

Dieterich, J. H. (1978). Time-dependent friction and the mechanics of stick-slip. *pure and applied geophysics*, *116*, 790–806. Retrieved from `https://doi.org/10.1007/BF00876539` doi: 0.1007/BF00876539

Dieterich, J. H. (1979). Modeling of rock friction: 1. experimental results and constitutive equations. *Journal of Geophysical Research: Solid Earth*, *84*(B5), 2161-2168. Retrieved from `https://agupubs.onlinelibrary.wiley.com/doi/abs/10.1029/JB084iB05p02161` doi: 10.1029/JB084iB05p02161

Dieterich, J. H. (1981). Constitutive properties of faults with simulated gouge. In *Mechanical behavior of crustal rocks* (p. 103-120). American Geophysical Union (AGU). Retrieved from `https://agupubs.onlinelibrary.wiley.com/doi/abs/10.1029/GM024p0103` doi: 10.1029/GM024p0103

Dobereiner, L., & Freitas, M. H. D. (1986). Geotechnical properties of weak sandstones. *Géotechnique*, *36*(1), 79-94. Retrieved from `https://doi.org/10.1680/geot.1986.36.1.79` doi: 10.1680/geot.1986.36.1.79

Edwards, B., Kraft, T., Cauzzi, C., Kästli, P., & Wiemer, S. (2015). Seismic monitoring and analysis of deep geothermal projects in St Gallen and Basel, Switzerland. *Geophysical Journal International*, *201*(2), 1022-1039. Retrieved from https://doi.org/10.1093/gji/ggv059 doi: 10.1093/gji/ggv059

Fang, Y., Elsworth, D., Ishibashi, T., & Zhang, F. (2018). Permeability Evolution and Frictional Stability of Fabricated Fractures With Specified Roughness. *Journal of Geophysical Research: Solid Earth*, *123*, 9355–9375. doi: 10.1029/2018JB016215

Farzadi, A., Waran, V., Solati-Hashjin, M., Rahman, Z. A. A., Asadi, M., & Osman, N. A. A. (2015). Effect of layer printing delay on mechanical properties and dimensional accuracy of 3D printed porous prototypes in bone tissue engineering. *Ceramics International*, *41*(7), 8320–8330. Retrieved from http://dx.doi.org/10.1016/j.ceramint.2015.03.004 doi: 10.1016/j.ceramint.2015.03.004

Gomez, J. S. (2017). *Mechanical Properties Characterization of Printed Reservoir Sandstone Analogues* (Master's thesis, University of Alberta). Retrieved from https://era.library.ualberta.ca/items/49660e82-3446-4a9a-9a74-e5ff2ab38470/download/7e82347e-42db-4031-bc32-12134e5441d7

Gomez, J. S., Chalaturnyk, R. J., & Zambrano-Narvaez, G. (2019). Experimental Investigation of the Mechanical Behavior and Permeability of 3D Printed Sandstone Analogues Under Triaxial Conditions. *Transport in Porous Media*, *129*(2), 541–557. Retrieved from https://doi.org/10.1007/s11242-018-1177-0 doi: 10.1007/s11242-018-1177-0

Head, D., & Vanorio, T. (2016). Effects of changes in rock microstructures on permeability: 3-D printing investigation. *Geophysical Research Letters*, *43*(14), 7494–7502. doi: 10.1002/2016GL069334.Received

Heslot, F., Baumberger, T., Perrin, B., Caroli, B., & Caroli, C. (1994). Creep, stick-slip, and dry-friction dynamics: Experiments and a heuristic model. *Physical Review E*, *49*(6), 4973–4988. doi: 10.1103/PhysRevE.49.4973

Huang, T., Chang, C., & Chao, C. (2002). Experimental and mathematical modeling for fracture of rock joint with regular asperities. *Engineering Fracture Mechanics*, *69*(17), 1977 - 1996. Retrieved from http://www.sciencedirect.com/science/article/pii/S0013794402000723 doi: https://doi.org/10.1016/S0013-7944(02)00072-3

Indraratna, B., Thirukumaran, S., Brown, E. T., & Zhu, S.-p. (2015). Modelling the Shear Behaviour of Rock Joints with Asperity Damage Under Constant Normal Stiffness. *Rock Mechanics and Rock Engineering*, *48*, 179–195. doi: 10.1007/s00603-014-0556-2

Ishibashi, T., Fang, Y., Elsworth, D., Watanabe, N., & Asanuma, H. (2020). Hydromechanical properties of 3D printed fractures with controlled surface roughness : Insights into shear-permeability coupling processes. *International Journal of Rock Mechanics and Mining Sciences*, *128*(February), 104271. Retrieved from https://doi.org/10.1016/j.ijrmms.2020.104271 doi: 10.1016/j.ijrmms.2020.104271

Jones, L. (2018). *The big ones: How natural disasters have shaped us (and what we can do about them)*. Doubleday. (ISBN 978-178578-436-1)

King, C.-Y. (1975). Model seismicity and faulting parameters. *Bulletin of the Seismological Society of America*, *65*(1), 245-259. Retrieved from https://pubs.geoscienceworld.org/bssa/article-pdf/65/1/245/2699375/BSSA0650010245.pdf

Kirkpatrick, J. D., Edwards, J. H., Verdecchia, A., Kluesner, J. W., Harrington, R. M., & Silver, E. A. (2020). Subduction megathrust heterogeneity characterized from 3D seismic data. *Nature Geoscience*. Retrieved from http://dx.doi.org/10.1038/s41561-020-0562-9 doi: 10.1038/s41561-020-0562-9

Knuth, M., & Marone, C. (2007). Friction of sheared granular layers: Role of particle dimensionality, surface roughness, and material properties. *Geochemistry, Geophysics, Geosystems*, *8*(3). doi: 10.1029/2006GC001327

Kozicki, J., Niedostatkiewicz, M., Tejchman, J., & Muhlhaus, H.-B. (2013). Discrete modelling results of a direct shear test for granular materials versus FE results. *Granular Matter*, *15*, 607–627. doi: 10.1007/s10035-013-0423-y

Li, Y., Oh, J., Mitra, R., & Hebblewhite, B. (2016). A constitutive model for a laboratory rock joint with multi-scale asperity degradation. *Computers and Geotechnics*, *72*, 143–151. doi: 10.1016/j.compgeo.2015.10.008

Marone, C., Raleigh, C. B., & Scholz, C. H. (1990). Frictional behavior and constitutive modeling of simulated fault gouge. *Journal of Geophysical Research: Solid Earth*, *95*(B5), 7007-7025. doi: 10.1029/JB095iB05p07007

Marone, C., & Scholz, C. (1989). Particle-size distribution and microstructures within simulated fault gouge. *Journal of Structural Geology*, *11*(7), 799 - 814. Retrieved from `http://www.sciencedirect.com/science/article/pii/0191814189900990` (Friction phenomena in rock) doi: https://doi.org/10.1016/0191-8141(89)90099-0

Mitra, S., El Mansori, M., Rodríguez, A., Castro, D., & Costin, M. (2019). Study of the evolution of transport properties induced by additive processing sand mold using X-ray computed tomography. *Journal of Materials Processing Tech.*, *227*(116495), 1–15. Retrieved from `https://doi.org/10.1016/j.jmatprotec.2019.116495` doi: 10.1016/j.jmatprotec.2019.116495

Mitra, S., Rodríguez de Castro, A., & El Mansori, M. (2018). The effect of ageing process on three-point bending strength and permeability of 3D printed sand molds. *International Journal of Advanced Manufacturing Technology*, *97*(1-4), 1241–1251. doi: 10.1007/s00170-018-2024-8

Mitra, S., Rodríguez de Castro, A., & El Mansori, M. (2019). On the rapid manufacturing process of functional 3D printed sand molds. *Journal of Manufacturing Processes*, *42*(March), 202–212. Retrieved from `https://doi.org/10.1016/j.jmapro.2019.04.034` doi: 10.1016/j.jmapro.2019.04.034

Newland, P. L., & Allely, B. H. (1957). Volume changes in drained taixial tests on granular materials. *Géotechnique*, *7*(1), 17-34. Retrieved from `https://doi.org/10.1680/geot.1957.7.1.17` doi: 10.1680/geot.1957.7.1.17

Papamichos, E., Tronvoll, J., Vardoulakis, I., Labuz, J. F., Skjærstein, A., Unander, T. E., & Sulem, J. (2000). Constitutive testing of Red Wildmoor sandstone Constitutive testing of Red Wildmoor sandstone. *Mechanics of Cohesive-Frictional Materials*, *5*, 1–40. doi: 10.1002/(SICI)1099-1484(200001)5

Patton, F. D. (1966). Multiple modes of shear failure in rock. In *Proc. 1st congr. int. soc. rock mech.* (pp. 509–513). Lisbon. Retrieved from `https://www.onepetro.org/conference-paper/ISRM-1CONGRESS-1966-087`

Pereira, J. P., & de Freitas, M. H. (1993). Mechanisms of Shear Failure in Artificial Fractures of Sandstone and Their Implication for Models of Hydromechanical Coupling. *Rock Mechanics and Rock Engineering*, *26*, 195–214. doi: 10.1007/BF01040115

Pimienta, L., Fortin, J., & Guéguen, Y. (2015). Experimental study of Young's modulus dispersion and attenuation in fully saturated sandstones. *Geophysics*, *80*(5), L57-L72. Retrieved from `https://doi.org/10.1190/geo2014-0532.1` doi: 10.1190/geo2014-0532.1

Popov, V. L., Grzemba, B., Starcevic, J., & Popov, M. (2012). Rate and state dependent friction laws and the prediction of earthquakes: What can we learn from laboratory models? *Tectonophysics*, *532-535*, 291–300. doi: 10.1016/j.tecto.2012.02.020

Power, W. L., Tullis, T. E., & Weeks, J. D. (1988). Roughness and wear during brittle faulting. *Journal of Geophysical Research: Solid Earth*, *93*(B12), 15268-15278. Retrieved from `https://agupubs.onlinelibrary.wiley.com/doi/abs/10.1029/JB093iB12p15268` doi: 10.1029/JB093iB12p15268

Primkulov, B., Chalaturnyk, J., Chalaturnyk, R., & Narvaez, G. Z. (2017). 3D Printed Sandstone Strength : Curing of Furfuryl Alcohol Resin-Based Sandstones. *3D Printing and Additive Manufacturing*, *4*(3), 149–155. doi:

10.1089/3dp.2017.0032
Queener, C., Smith, T., & Mitchell, W. (1965). Transient wear of machine parts. *Wear*, *8*(5), 391 - 400. Retrieved from http://www.sciencedirect.com/science/article/pii/0043164865901705 doi: https://doi.org/10.1016/0043-1648(65)90170-5
Raleigh, C. B., Healy, J. H., & Bredehoeft, J. D. (1976). An Experiment in Earthquake Control at Rangely, Colorado. *Science*, *191*(4233), 1230–1237. Retrieved from http://www.sciencemag.org/cgi/doi/10.1126/science.191.4233.1230 doi: 10.1126/science.191.4233.1230
Rattez, H., Stefanou, I., & Sulem, J. (2018a). The importance of Thermo-Hydro-Mechanical couplings and microstructure to strain localization in 3D continua with application to seismic faults. Part I: Theory and linear stability analysis. *Journal of the Mechanics and Physics of Solids*, *115*(March), 54–76. Retrieved from https://linkinghub.elsevier.com/retrieve/pii/S0022509617309626 doi: 10.1016/j.jmps.2018.03.004
Rattez, H., Stefanou, I., Sulem, J., Veveakis, M., & Poulet, T. (2018b). The importance of Thermo-Hydro-Mechanical couplings and microstructure to strain localization in 3D continua with application to seismic faults. Part II: Numerical implementation and post-bifurcation analysis. *Journal of the Mechanics and Physics of Solids*, *115*, 1–29. Retrieved from https://linkinghub.elsevier.com/retrieve/pii/S0022509617309638 doi: 10.1016/j.jmps.2018.03.003
Renard, F., Mair, K., & Gundersen, O. (2012). Surface roughness evolution on experimentally simulated faults. *Journal of Structural Geology*, *45*, 101–112. Retrieved from http://dx.doi.org/10.1016/j.jsg.2012.03.009 doi: 10.1016/j.jsg.2012.03.009
Roscoe, K. H. (1970). The influence of strains in soil mechanics. *Géotechnique*, *20*(2), 129-170. Retrieved from https://doi.org/10.1680/geot.1970.20.2.129 doi: 10.1680/geot.1970.20.2.129
Rosenau, M., Corbi, F., & Dominguez, S. (2017). Analogue earthquakes and seismic cycles: experimental modelling across timescales. *Solid Earth*, *8*(3), 597-635. Retrieved from https://hal.archives-ouvertes.fr/hal-01553120 doi: 10.5194/se-8-597-2017
Sadrekarimi, A., & Olson, S. M. (2010). Shear band formation observed in ring shear tests on sandy soils. *Journal of Geotechnical and Geoenvironmental Engineering*, *136*(2), 366-375. Retrieved from https://ascelibrary.org/doi/abs/10.1061/%28ASCE%29GT.1943-5606.0000220 doi: 10.1061/(ASCE)GT.1943-5606.0000220
Schallamach, A. (1971). How does rubber slide? *Wear*, *17*(4), 301 - 312. Retrieved from http://www.sciencedirect.com/science/article/pii/0043164871900330 doi: https://doi.org/10.1016/0043-1648(71)90033-0
Schmittbuhl, J., Gentier, S., & Roux, S. (1993). Field measurements of the roughness of fault surfaces. *Geophysical Research Letters*, *20*(8), 639–641. doi: 10.1029/93GL00170
Scholz, C. (2002). *The Mechanics of Earthquakes and Faulting* (2nd ed.). New York: Cambridge University Press. doi: 10.1017/CBO9780511818516
Schumacher, M., Deisinger, U., Detsch, R., & Ziegler, G. (2010). Indirect rapid prototyping of biphasic calcium phosphate scaffolds as bone substitutes : influence of phase composition , macroporosity and pore geometry on mechanical properties. *Journal of Materials Science: Materials in Medicine*, *21*, 3119–3127. doi: 10.1007/s10856-010-4166-6
Scuderi, M. M., Collettini, C., & Marone, C. (2017). Frictional stability and earthquake triggering during fluid pressure stimulation of an experimental fault. *Earth and Planetary Science Letters*, *477*, 84–96. doi: 10.1016/j.epsl.2017.08.009

Stefanou, I. (2019). Controlling anthropogenic and natural seismicity: Insights from active stabilization of the spring-slider model. *Journal of Geophysical Research: Solid Earth*, *124*(8), 8786-8802. Retrieved from `https://agupubs.onlinelibrary.wiley.com/doi/abs/10.1029/2019JB017847` doi: 10.1029/2019JB017847

Tinti, E., Scuderi, M. M., Scognamiglio, L., Di Stefano, G., Marone, C., & Collettini, C. (2016). On the evolution of elastic properties during laboratory stick-slip experiments spanning the transition from slow slip to dynamic rupture. *Journal of Geophysical Research: Solid Earth*, *121*(12), 8569-8594. Retrieved from `https://agupubs.onlinelibrary.wiley.com/doi/abs/10.1002/2016JB013545` doi: 10.1002/2016JB013545

Tzortzopoulos, G., Stefanou, I., & Braun, P. (2019). Designing Experiments for Controlling earthQuakes (CoQuake) by Fluid Injection. In *12th hstam 2019 international congress on mechanics.* Thessaloniki, Greece.

Upadhyay, M., Sivarupan, T., & El Mansori, M. (2017). 3D printing for rapid sand casting—A review. *Journal of Manufacturing Processes*, *29*, 211–220. Retrieved from `http://dx.doi.org/10.1016/j.jmapro.2017.07.017` doi: 10.1016/j.jmapro.2017.07.017

Vaezi, M., & Chua, C. K. (2011). Effects of layer thickness and binder saturation level parameters on 3D printing process. *The International Journal of Advanced Manufacturing Technology*, *53*, 275–284. doi: 10.1007/s00170-010-2821-1

Vardoulakis, I., & Graf, B. (1985). Calibration of constitutive models for granular data from biaxial experiments materials using data from biaxial experiments. *Géotechnique*, *35*(3), 299–317. doi: 10.1680/geot.1985.35.3.299

Vlasea, M., Pilliar, R., & Toyserkani, E. (2015). Control of Structural and Mechanical Properties in Bioceramic Bone Substitutes via Additive Manufacturing Layer Stacking Orientation. *Additive Manufacturing*, *6*, 30–38. Retrieved from `http://dx.doi.org/10.1016/j.addma.2015.03.001` doi: 10.1016/j.addma.2015.03.001

Wood, D. M. (1991). Plasticity and yielding. In *Soil behaviour and critical state soil mechanics* (p. 55–83). Cambridge University Press. doi: 10.1017/CBO9781139878272.004

Zhao, Z. (2013). Gouge Particle Evolution in a Rock Fracture Undergoing Shear : a Microscopic DEM Study. *Rock Mechanics and Rock Engineering*, *46*, 1461–1479. doi: 10.1007/s00603-013-0373-z